Università degli Studi
di Modena e Reggio Emilia

Dipartimento di Ingegneria "Enzo Ferrari"

Dottorato di ricerca in
ING-IND/10 Fisica Tecnica Industriale

Scuola di dottorato in
High Mechanics and Automotive Design & Technology
XXV ciclo

Numerical studies of turbulent forced convection in a wavy channel for low and order one Prandtl number

Candidato: Orsola Errico

Relatore: Dott. Enrico Stalio

Direttore della scuola di dottorato: Prof. Paolo Tartarini

Anno Accademico 2011/2012

a Gianni

Ci sedemmo dalla parte del torto visto che tutti gli altri posti erano occupati.

Bertolt Brecht

Acknowledgments

The research study described in the present thesis has been developed in the last three-year period 2010-2012. The research topic, dealing with numerical simulations of turbulent heat trasfer in separated flows and for low Prandtl number to order of unity, is currently of great interest both for industrial applications and scientific research.

I am grateful to the supervisor of my doctoral course, Dr. Enrico Stalio, for his contribution to my studies and his guidance during the last three years.

I wish to thank Prof. Giovanni Barozzi and Prof. Mauro Corticelli for their always support and wise advices.

My thanks go to Dr. Diego Angeli and Dr. Marco Cavazzuti for contributing to the application of RANS method to the present investigations, and for all the interesting discussions we had on different research topics.

Finally I sincerely thank my family and all my friends!

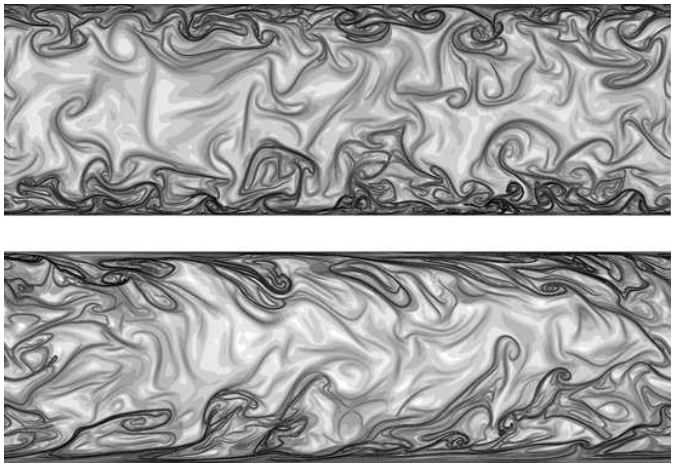

"Turbulent Channel structures".
Art of Science, Gallery 2006. Melissa Green.
Princeton University.

Contents

Notation

a	wave amplitude
A	cross-sectional area
c	specific heat
D_h	hydraulic diameter
f	friction factor
h	heat transfer coefficient
H	maximum wavy wall channel height
H_av	average channel height
k	turbulent kinetic energy
$\mathbf{I}$	unit diadic $\mathbf{I} = (100; 010; 001)$
L_x,L_y,L_z	length of the domain in x, y, z direction
L	periodic length in x direction
$\dot{m}$	mass flow rate
n	coordinate normal to the wall surface
N_x,N_y,N_z	number of grid points in x, y, z direction
Nu	Nusselt number
p	periodic part of the pressure field, also wet perimeter
P	pressure field
Pr	molecular Prandtl number, $Pr = \nu/\alpha$
q	square-root of turbulent kinetic energy $q = \sqrt{k}$
Q_s	time-averaged volume flow rate per unit spanwise width of the channel

Re	Reynolds number, $Re = D_h\, u_m/\nu$
Re^*	Reynolds number of the reference velocity, $Re^* = u^*\,\delta/\nu$
Re_τ	Reynolds number of the friction velocity, $Re_\tau = u_\tau\,\delta/\nu$
$\overline{S_{ij}}$	mean rate of strain $\overline{S}_{ij} = \frac{1}{2}\left(\frac{\partial \overline{u}_i}{\partial x_j} + \frac{\partial \overline{u}_i}{\partial x_j}\right)$
S_w	wall surface
T	temperature field
T_w	wall temperature
T_b	bulk temperature
$T_{b,in}$	bulk temperature at the channel inlet
t	time
t^*	reference time, $t^* = \delta/u^*$
u	streamwise velocity component
$\mathbf{u}$	velocity vector
u^*	reference velocity, $u^* = \beta\delta/\rho$
u_τ	friction velocity, $u_\tau = \tau_w/\rho$
u_m	mean velocity, $u_m \equiv Q_s/H_{\mathrm{av}}$
v	vertical velocity component
V	averaging volume
w	spanwise velocity component
$\mathbf{x}$	unit vector for the spatial coordinate
x, y, z	streamwise, vertical, and spanwise coordinate

Greek letters

α	thermal diffusion coefficient $\alpha = k/\rho c$
α_t	eddy diffusivity
β	pressure drop assigned along x
δ	half the average channel height
δ_{ij}	Kronecker delta
ϵ	dissipation rate of turbulent kinetic energy
η	curvilinear coordinate in direction normal to the wall
λ	periodic length, wavelength
Λ	temperature decay rate along x
Λ_L	temperature decay rate along the periodic length L
ν	kinematic viscosity
ν_t	eddy viscosity
ω	specific dissipation rate $\omega = \epsilon/k$
θ	periodic temperature variable
ξ	curvilinear coordinate in direction tangential to the wall
ρ	density
$\tau_{w,u}$, $\tau_{w,l}$	wall shear stress of the upper and lower wall
ζ	dissipation rate of q

Subscripts

b	bulk
m	mean
w	wall
w, u	upper wall
w, l	lower wall
τ	friction value

Superscripts

$\bullet'$	fluctuating value
$\bullet^+$	wall units
$\overline{\bullet}$	time averaged value
$\langle\bullet\rangle$	spatial average

Chapter 1

Introduction

Liquid metals can be used for many engineering applications, as for the design of advanced nuclear reactors, where they are often employed as coolants. The high thermal conductivity of liquid metals, and hence their low molecular Prandtl number, imply that the molecular thermal conduction in metal fluids is significant not only in the near-wall layer, but also in the core flow. The thermal boundary layer in a liquid-metal flow is thicker with respect to a non-metal flow and develops faster with respect to the dynamic boundary layer. These features, together with the high thermal capacity and low kinematic viscosity of liquid metals allow for a great heat transfer efficiency. The use of liquid metals in cooling systems also provides safety advantages due to their high boiling point, and the quick solidification in case of leak. Moreover they allow for the use of magnetohydrodynamics pumps, instead of moving machines. However reliable physical models of convective heat transfer in liquid metals are still lacking. A detailed knowledge of velocity and thermal fields is needed for model development and it is almost impossible to obtain through

experiments, because of the opacity of these fluids and the care required in handling them. Numerical simulation is a valuable tool for investigating heat and mass transfer in low-Prandtl number flows. In the last twenty years a large number of numerical studies have been conducted in this field, but in the fundamental case of flat channel flow, as in (Kawamura et al. 1998), (Na et al. 1999), (Kawamura et al. 2004), (Kozuka et al. 2009).

Figure 1.1: Wavy groove heat exchanger.

Periodic, corrugated geometries are very common in heat exchangers as they promote heat transfer through turbulent mixing. The flow over such geometries is characterized by separation and reattachment phenomena, which are beneficial for heat transfer enhancement. Wavy surfaces are largely used in heat transfer devices, an example is shown in figure 1.1, and a number of work are available in the literature dealing with flows over wavy surfaces, both experimental works, as (Zilker and Hanratty 1979), (Hudson 1993), (Hudson et al. 1996), (Kuhn et al. 2008), and numerical, as (Maaß and Schumann 1996), (Patel et al. 1991), (Cherukat et al. 1998), (Choi and

Suzuki 2005), (Rossi 2010), (Dellil et al. 2004).

The present thesis deals with a numerical study of turbulent forced convection in a channel with a top flat wall and a bottom wavy wall, for different Prandtl numbers. The Reynolds number investigated is Re = 19 000, based on the mean bulk velocity and hydraulic diameter. Three different values are considered for the Prandtl number: a very low-Prandtl number, Pr = 0.025, which corresponds to the liquid Lead-Bismuth Eutectic, a order one Prandtl number, Pr = 0.71, which corresponds to air, and an intermediate value between these two, Pr = 0.2, which is one of the lowest Prandtl number for a gas and corresponds to a Helium-Xenon gas mixture.

Direct numerical simulation (DNS) and Reynolds-Averaged Navier-Stokes (RANS) methods have been used for the numerical simulations, being the first method the most rigorous for investigating turbulence, but also the most demanding in terms of computational costs, and the second one the largely used in common practice, being much less elaborate and much less expansive in terms of CPU. DNSs are performed by means of a home-made code and the RANS simulations by using the OpenFOAM 2.0.1 CFD package.

This study aims at investigating on the combined effects of the wavy wall shape and of the Prandtl number from low to unit values, on the turbulent heat transport mechanisms. Direct simulations are performed to this end. Moreover, by means of RANS simulations, it aims to assess the performance of the two different eddy-viscosity models, k-ω SST model (Menter 1993) and q-ζ model (Gibson and Dafa'Alla 1995), selected for their good characteristics.

The thesis includes eight chapters. The current chapter 1

is to introduce to the subject of the work and to describe the way the thesis is organized in the different chapters.

In the chapter 2 the main characteristics of turbulent flows are briefly discussed, as well as the possible solutions to the problem of the simulation of turbulence. The numerical methods selected for the present study are introduced, the DNS method and the RANS method, by discussing on their fundamentals, and their main advantages and disadvantages.

The chapter 3 focuses on the problem statement: the geometry of the problem and the assumptions on the flow regime and fluid properties are presented first, thus establishing the physics of the problem. To follow, the computational domain and the set of boundary conditions considered for the numerical simulations are described. Finally, the governing equations for mass, momentum and energy are written and the non-dimensional key parameters are defined.

Chapter 4 is concerned with the numerical methods employed for the solution of the governing equations. The DNS method is discussed first: the numerical techniques adopted for the present DNS simulations are described, the details of the mesh type and grid spacings used for the domain discretization are provided, and also a schematic description of the numerical procedure used in code for the solution of the governing equations, and details on the numerical schemes adopted for the temporal and spatial discretization. Subsequently, the RANS method is described. The two eddy-viscosity models selected for RANS simulations, the k-ω SST model (Menter 1993) and the q-ζ model (Gibson and Dafa'Alla 1995), are presented, as well as the standard-gradient transport model used in the RANS simulations for the modeling of the eddy-diffusivity. The mesh used for the domain discretiza-

tion and the numerical procedures adopted for the solution of the equations are provided also in this case, as done for the DNS case.

In the chapter 5 the validation study conducted for the DNS method is presented. For the validation of the DNS method a direct simulation for a Reynolds number of Re = 13 700 based on the mean velocity and the hydraulic diameter has been performed, which is comparable to those of reference data, the experiments by Hudson (1993) and DNS data by Cherukat et al. (1998), available for the velocity field. The profiles of the main averaged quantities and first order moments are successfully compared with both the experiments and previous DNS data.

In the chapter 6 the results obtained by DNSs at Re = 19 000 are presented. Results are provided for the velocity field and for the three different thermal fields corresponding to the different Prandtl numbers investigated. The main focus is on the flow separation effects and Prandtl number effects on the turbulent heat transport mechanisms. Maps of the instantaneous velocity field are displayed both in the longitudinal plane and cross-sections of the channel, also the streamlines and the profiles of the time-averaged velocity field are represented, as well as the profiles of the root-mean-square of velocity fluctuations and Reynolds stress. Moreover, a quadrant-hole analysis of Reynolds stress is conducted, thus identifying the relative contribution of four quadrants –corresponding to four different types of event– to the formation of statistics. The global value of the friction factor is provided, and it is compared with reference values for the flat channel case. Maps of the instantaneous temperature fields are displayed for different cross-sections of the channel, and the profiles of the

time-averaged temperature fields are represented. For comparative purposes the profile of the mean temperature fields in the flat wall region is depicted together with the DNS results by Kawamura et al. (1998), and the log-law for the thermal field by Kader and Yaglom (1972). The profiles of the root-mean-square of temperature fluctuations and turbulent heat fluxes are drawn and, as for the Reynolds stress, a quadrant-hole analysis is performed for the turbulent heat fluxes. The local and global values of the Nusselt number are given. Maps of turbulent Prandtl number are depicted in the lower region of the channel, while an x-averaged profile of turbulent Prandtl number is drawn in the region close to the upper flat wall. Finally the performance of some different turbulence diffusion models is assessed against the DNS results.

The chapter 7 includes the results obtained by RANS simulations for $\mathrm{Re} = 19\,000$ and for $\mathrm{Pr} = 0.71$. The suitability of the two-equations eddy-viscosity turbulence models k-ω SST (Menter 1993) and q-ζ model (Gibson and Dafa'Alla 1995) for the present case study is evaluated by comparison with the results obtained by direct simulations. For comparative purposes the results provided by DNS are averaged over the time and the spanwise direction z. Streamlines and velocity contours as provided by the RANS simulations and DNSs are represented. The ability of the two selected viscosity models in the prediction the flow separation and reattachment positions, the size of the mean recirculation bubble, and the profile shape of turbulent kinetic energy and Reynolds stress is discussed. The contours of the thermal field and the profiles of the vertical turbulent heat flux are presented, and the global value of the heat transfer rate is also provided.

The last chapter contains the conclusions, encompassing the main results obtained in the present study.

Chapter 2

Numerical simulations of turbulence

Turbulent flow regime occurs in most of engineering applications, and the effectiveness of the turbulent transport of momentum, heat and mass is of a primary importance in many of these applications, as in heat transfer devices.

The main characteristics of turbulent flows are briefly discussed in the following, as well as the problem of numerical simulation of turbulence, before introducing the two numerical methods selected for the present study: the DNS method and the RANS method.

Turbulent flows are characterized by chaotic property changes. Turbulent variables are strongly and irregularly varying both in time and space, and in all the three spatial dimensions. The turbulent fluctuations occur on a broad range of time scales and length scales. The largest scale of motion, known as *integral scale* L, is comparable to the domain size, it contains the most of the energy and controls the transport and mixing. The energy contained by the largest eddies is then transferred

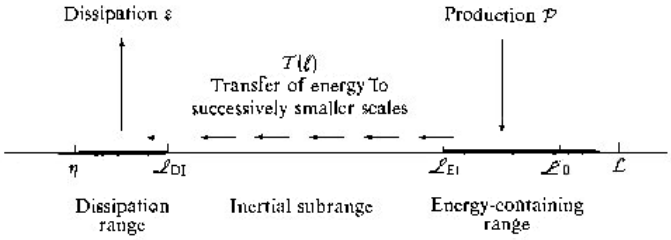

Figure 2.1: A schematic diagram of energy cascade by Pope (2000). l_{DI} and l_{EI} indicate, respectively, the demarcation line between the dissipation (D) and inertial (I) subranges, and the energy (E) and inertial (I) subranges.

to smaller and smaller eddies, until it is dissipated by viscosity. The scale of the smallest eddies is known as *Kolmogorov scale* η, and it is almost entirely determined by the rate at which it receives energy from the large scales, and by the viscosity. The *inertial subrange* is instead the range of scales corresponding to the *energy cascade*, the process of transferring energy from the largest and unstable eddies to successively smaller eddies until the smallest eddies of the Kolmogorov scale. As the Reynolds number increases the difference between the integral scale and the Kolmogorov scale becomes larger. A schematic diagram of energy cascade is given in figure 2.1, by Pope (2000). A further important characteristic of turbulence is the vorticity, for instance the stretching of three-dimensional vortices is one of the principal mechanisms which increases the turbulence intensity. The turbulent diffusivity also plays an important role for accomplishing the turbulent mixing and enhancing the momentum, heat and mass transfer rates. Turbulent flows are furthermore highly dissipative, shear stress rapidly dissipate the kinetic energy, which is irre-

versibly converted into internal energy.

Numerical simulations of turbulent flows, which are three-dimensional, time-depending and random, with a wide range of time scales and length scales, represent a difficult task in the field of numerical simulations. The mass, momentum and energy conservation equations of the instantaneous field have to be solved. For incompressible flow of a Newtonian fluid with constant thermophysical properties they read:

$$\frac{\partial u_j}{\partial x_j} = 0 \tag{2.1}$$

$$\frac{\partial u_i}{\partial t} + \frac{\partial (u_j u_i)}{\partial x_j} = -\frac{1}{\rho}\frac{\partial P}{\partial x_i} + \nu \frac{\partial^2 u_i}{\partial x_j^2} \tag{2.2}$$

$$\frac{\partial T}{\partial t} + u_j \frac{\partial T}{\partial x_j} = \alpha \frac{\partial^2 T}{\partial x_j^2} \tag{2.3}$$

In numerical simulations the instantaneous behavior of turbulent variables is commonly treated following a Reynolds decomposition, which separates the mean value from the fluctuating part of such variables:

$$\mathbf{u}(\mathbf{x}, t) = \overline{\mathbf{u}}(\mathbf{x}) + \mathbf{u}'(\mathbf{x}, t) \tag{2.4}$$

$$T(\mathbf{x}, t) = \overline{T}(\mathbf{x}) + T'(\mathbf{x}, t) \tag{2.5}$$

Due to the fluctuations, transport mechanisms originate from the advection term of the Navier-Stokes and energy equations. The contributions appearing in the non-linear acceleration term of the momentum conservation equation have dimension of stress and are conventionally referred to as Reynolds

stress, $\overline{u_i' u_j'}$, while the contributions appearing in the energy conservation equation are referred as turbulent scalar fluxes $\overline{u_i' T'}$. Reynolds stress and the turbulent scalar fluxes represent the only difference between the conservation equations for instantaneous quantities and averaged quantities:

$$\frac{\partial \overline{u}_j}{\partial x_j} = 0 \tag{2.6}$$

$$\frac{\partial \overline{u}_j \overline{u}_i}{\partial x_j} = -\frac{1}{\rho}\frac{\partial \overline{P}}{\partial x_i} + \frac{\partial}{\partial x_j}\left(\nu \frac{\partial \overline{u}_i}{\partial x_j} - \overline{u_i' u_j'}\right) \tag{2.7}$$

$$\frac{\partial \overline{u}_j \overline{T}}{\partial x_j} = \frac{\partial}{\partial x_j}\left(\alpha \frac{\partial \overline{T}}{\partial x_j} - \overline{u_j' T'}\right) \tag{2.8}$$

2.1 DNS approach

Direct numerical simulations solve the mass, momentum and energy conservation equations of the instantaneous variables, without averaging or approximation other than numerical discretization, whose errors can be estimated and controlled. DNS represent the most rigorous method for investigating the flow dynamics and the heat transfer mechanisms in turbulent flows. By solving all turbulent scales, DNSs provide a precise description of the dynamic features and heat transfer mechanisms in turbulent flows. To this aim the computational domain and the mesh used for direct simulations have to be adequately designed: the computational domain has to be large enough to contain the largest turbulence eddies, therefore each linear dimension of the domain must be at least a

few times the integral scale, L, while in order to solve the dissipative scales the mesh size has to be of the same order of magnitude of the universal Kolmogorov scale, η. For homogeneous isotropic turbulence, the simplest to investigate, a uniform grid can be used and the number of grid points in each direction must be at least equal to the ratio between the integral scale and the Kolmogorov scale. This ratio can be shown proportional to $Re^{3/4}$, where Re is the Reynolds number based on the magnitude of velocity fluctuations and the integral scale. Also, an accurate time history is required. For the simplest homogeneous isotropic turbulence the number of time-step required is proportional to $Re^{3/4}$ (Pope 2000). The processing speed and the memory of the computer limit the number of grid points and time-step used in numerical simulations, so that DNSs can be performed only for relatively low Reynolds number values. Further, due to the very fine grid used in the near wall region, where turbulent eddies of very small size occur, numerical instability may originates from the viscous terms involving wall-normal derivatives, so these terms have been often treated implicitly. Another difficulty in DNSs is the assignment of initial and boundary conditions. The effects of initial conditions influence the flow for a considerable time, usually a few "eddy-turnover times", which corresponds to the integral time-scale, and so that the first part of simulation that is started with artificial initial conditions must be discarded being not physical. For channel flow the best choice for initial condition has been found to be a mixture of the mean velocity, instability modes and noise. Similar considerations can be applied to the boundary conditions at the inflow of the domain. Direct simulation must be run for some time before the flow develops all of the cor-

rect characteristics of the physical flow. This time strictly depends on the physics of the turbulent flow. In separated flows, there are regions that communicate with the remainder of the flow on a very long time scale and the development process can be very slow, making very long run time necessary. Due to the high computational cost DNSs can not be used as design tool, and also the detailed descriptions in time and space provided by DNS are often not needed for design purposes. DNSs rather represent a research tool, which allows for statistical information and database construction.

2.2 RANS approach

Differently from DNS, the Reynolds-Averaged-Navier-Stokes approach is largely used in common practice, due to its lower computational cost. In this case the time-averaged conservation equations are solved, equations (2.6), (2.7), (2.8). The additional terms included in these averaged equations, the Reynolds stress and the turbulent scalar fluxes, introduce new unknowns, so that additional equations are needed for the closure of the problem. RANS methods are distinguished into two different type on the base of the approach they use to solve the turbulence closure problem. The RANS methods based on the Reynolds stress model (RSM), which solve transport equations for all the Reynolds stress components, not really largely used as still quite complicate, and the RANS methods based on the Bussinesq hypothesis, which are instead less elaborate and largely employed. The Boussinesq hypothesis assumes that the deviatoric Reynolds stress, $-\overline{u_i' u_j'} + 2/3k\delta_{ij}$, is proportional to the mean rate of strain $\overline{S}_{ij} = 1/2\,(\partial\overline{u}_i/\partial x_j + \partial\overline{u}_j/\partial x_i)$. It is formulated as follows:

$$-\overline{u_i' u_j'} + \frac{2}{3} k \delta_{ij} = 2\nu_t \overline{S}_{ij} \tag{2.9}$$

where the positive scalar coefficient ν_t is the turbulent viscosity, also called *eddy-viscosity*. The momentum equation for the averaged variables incorporating the turbulent-viscosity hypothesis is:

$$\frac{\partial \overline{u}_j \overline{u}_i}{\partial x_j} = -\frac{1}{\rho}\frac{\partial}{\partial x_i}\left(\overline{P} + \frac{2}{3}\rho k\right) + \frac{\partial}{\partial x_j}\left[(\nu + \nu_t)\frac{\partial \overline{u}_i}{\partial x_j}\right] \tag{2.10}$$

where $(\nu + \nu_t)$ is known as the effective viscosity, ν_{eff}, and $(\overline{P} + 2/3\rho k)$ as the modified pressure.

The unit of ν_t is the same of the molecular viscosity, and because it is added to the molecular viscosity in the averaged momentum equation it is known as *eddy-viscosity*. The Boussinesq hypothesis implies an isotropic turbulence, and a proportional relation between the Reynolds stress and the strain rate, which are not valid in general. However these assumptions considerably simplify the turbulence closure problem and the computer demands decrease substantially. Also, the RANS eddy-viscosity turbulence models perform reasonable in many flow cases, not really in the more complex flows, where strong flow acceleration or deceleration occur, or for example where the curvature effects are significant. Eddy-viscosity turbulence models (EVMs) are differently accurate depending on how they model the eddy-viscosity: the coefficients they use, the functions they use for damping ν_t in the near-wall region, and the set of boundary conditions. They are fundamentally distinguished into three classes: the simplest zero-equations EVMs, which include an algebraic relation for ν_t, and the more accurate one-equation models and

even more accurate two-equation models, which solve extra transport equations of turbulence scalar variables for the modeling of ν_t. The two-equation EVMs are of the most used turbulence models in industrial design. Fundamental models are the standard k-ϵ model developed by Launder and Sharma (1974), which solves the extra transport equations of the turbulent kinetic energy k and its dissipation rate ϵ, and k-ω model by Wilcox (1988), which solves the extra transport equations of the turbulent kinetic energy k and the specific dissipation ω. A number of two-equation EVMs are available today, being this kind of models easy to modify, tune and improve (Bredberg 2001) and probably new models will be introduced, considering the great interest of the applied research community in this issue, especially into extent the suitability of such simple models to the more complex flow configurations.

For predictions of the temperature field, scalar fluxes models are needed in addition to the modeling of the turbulent velocity field. The standard gradient-transport model is the simplest model, numerically robust and largely used. It is based on the Simple Gradient Diffusion Hypothesis (SGDH), which assumes the scalar flux vector aligned with the mean scalar gradient:

$$\overline{u_i' T'} = -\alpha_t \frac{\partial \overline{T}}{\partial x_i} \tag{2.11}$$

where α_t is the isotropic *eddy-diffusivity*, which makes the scalar fluxes proportional, and therefore aligned, to the mean scalar gradient. However, this approach even for simple turbulent flows does not give realistic predictions, mainly as it does not account for the anisotropic character of turbulent scalar

fluxes, as for example proved by Corrsin (1974) and Kim and Moin (1989). An algebraic flux model, instead, consider an eddy-diffusivity tensor, which is generally nor diagonal neither symmetric, thus accounting for the anisotropy of the turbulent scalar fluxes. Among the algebraic flux models a number of formulation are available, some of them applied successfully also to complex flows, as in (Suga 2004), (Younis et al. 2007). A second-order full stress transport closure, which directly solves the transport equations of the turbulent stress, should provide more accurate predictions. However, as many studies demonstrate, e.g.(Wang et al. 2004), this is true only in some cases depending on the flow configuration, and this dissuades from the use of such a complex approach in industrial CFD practice.

In the present work DNSs are performed by use of a second-order finite volume code, home-made, and RANS simulations by use of OpenFOAM 2.0.1 CFD package. Two different two-equations eddy-viscosity turbulence models have been selected for RANS simulations: the Gibson's q-ζ model (Gibson and Dafa'Alla 1995), and the Shear-Stress Transport k-ω model (k-ω SST) (Menter 1993). The standard gradient transport model is used for the turbulent scalar fluxes modeling.
A description of the numerical methods employed is given in the chapter 3.

Chapter 3

Problem statement

The problem statement is provided in the following: the geometry of the problem and the assumptions on the flow regime and fluid properties are presented first, thus establishing the physics of the problem. In the following, the computational domain and the set of boundary conditions considered for the numerical simulations are described. Finally, the governing equations for mass, momentum and energy are presented both in dimensional and the non-dimensional form.

3.1 Geometry and assumptions

The geometry of the problem consists of a channel with a flat top wall and a wavy bottom wall, and it is unbounded in both the streamwise x and the spanwise direction z, as shown in figure 3.1, where the coordinate system of axes x y z and the main flow direction are also indicated.

The hypothesis of fully developed flow and thermal field is assumed. In the case of a channel with constant cross-flow area this means that the profile of the time-averaged

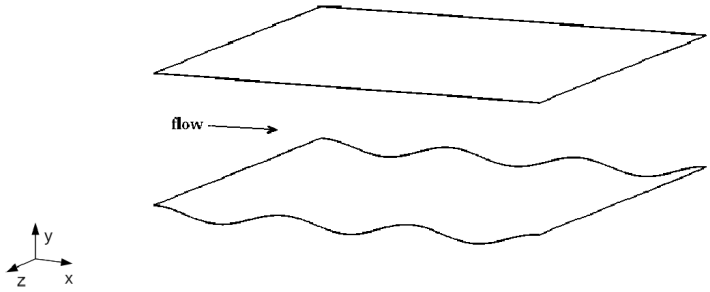

Figure 3.1: Geometry of the problem.

velocity field does not vary along the streamwise coordinate x (hydraulic development):

$$\frac{\partial \overline{\mathbf{u}}(x,y)}{\partial x} = 0$$

and that the time-averaged non-dimensional temperature $(\overline{T}(x,y) - \overline{T_w}(x))/(\overline{T_b}(x) - \overline{T_w}(x))$, where the bulk temperature $T_b = u_m^{-1} \int_A uTdA$, does not varies along x (thermal development):

$$\frac{\partial}{\partial x}\left[\frac{\overline{T}(x,y) - \overline{T}_w(x)}{\overline{T}_b(x) - \overline{T}_w(x)}\right] = 0$$

For a streamwise periodic channel flow, the hypothesis of periodically fully developed velocity field can be assumed, with similar profiles in x and $x + \lambda$, where λ is the periodic length (Patankar et al. 1977):

$$\overline{\mathbf{u}}(x,y) = \overline{\mathbf{u}}(x+\lambda, y)$$

Also, the periodic fully developed thermal conditions can be written as follows:

$$\frac{\overline{T}(x,y)-\overline{T}_w(x)}{\overline{T}_b(x)-\overline{T}_w(x)}=\frac{\overline{T}(x+\lambda,y)-\overline{T}_w(x+\lambda)}{\overline{T}_b(x+\lambda)-\overline{T}_w(x+\lambda)}$$

Numerical investigations of turbulent forced convection in the wavy channel flow have been performed for three different fluids: air, whose Prandtl number is $\mathrm{Pr}=0.71$, Helium-Xenon gas mixture with $\mathrm{Pr}=0.2$, and liquid Lead-Bismuth Eutectic with $\mathrm{Pr}=0.025$.

3.2 Computational domain and BCs

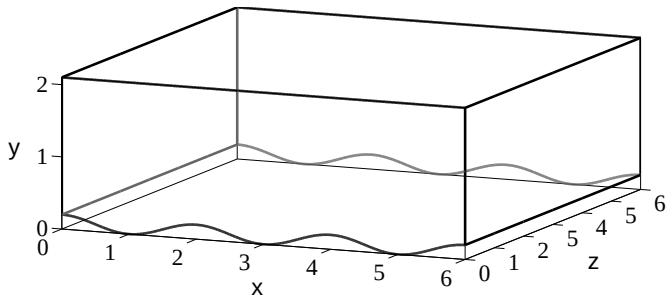

Figure 3.2: Three-dimensional computational domain of DNSs.

Numerical experiments are possible in a domain of finite volume. A three-dimensional computational domain, periodic in the streamwise direction and homogeneous in the spanwise direction is considered in this study to perform direct numerical simulations. The computational domain is depicted in figure 3.2, together with the coordinate system. For RANS sim-

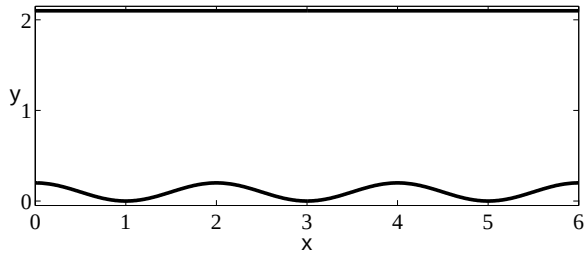

Figure 3.3: Two-dimensional computational domain of RANS.

ulations a two-dimensional domain is considered, which corresponds to the longitudinal section of the DNS 3D-domain, see figure 3.3.

The shape of the wavy wall y_w in the x - y plane is described by the function:

$$y_w = a \cos\left(\frac{2\pi x}{\lambda}\right) \tag{3.1}$$

where a is the amplitude of the wave and λ its wavelength, see figure 3.4. In the present investigations wavelength and amplitude are set equal to 2δ and 0.1δ, where δ corresponds to half the average channel height H_{av}. Geometrical parameters have been selected to match the geometry investigated in the experiments by Hudson (1993) and subsequent DNSs by Maaß and Schumann (1996) and Cherukat et al (1998).

As displayed in figure 3.2 and 3.3 the length of the computational domain in streamwise direction encompasses three periodicities, thus the domain size in x is $L_x = 6\delta$. It is smaller than the domain selected by Cherukat et al. (1998) as they perform the computations over four periodicities, but the smaller L_x employed does not spoil the accuracy of present

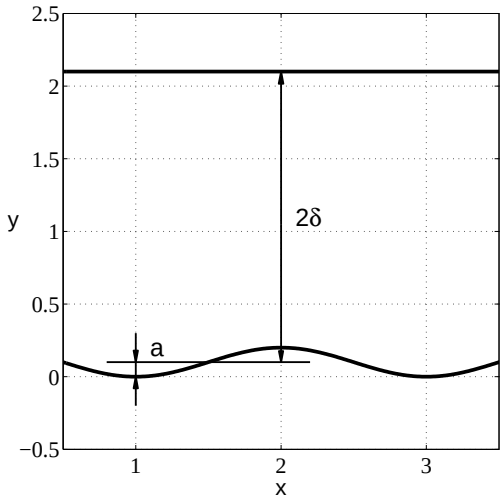

Figure 3.4: Details of the computational domain.

results, as demonstrated by validation in chapter 4 and also corroborated by the λ_2 analysis by Calhoun and Street (2001), who show that typical large scale structures have size in streamwise direction, $\lambda_x = \lambda$. The size of the domain in z is instead larger with respect to the domain selected by Cherukat et al. (1998), it is $L_z = 6\delta$ as required for simulating the low Prandtl number temperature fields.

The flow is driven by a constant pressure drop imposed in x direction. To simulate the flow over an infinite series of waves, periodic boundary conditions (BCs) are set both in the periodic streamwise direction and homogeneous spanwise direction. At walls no-slip BCs are assigned and a uniform and constant temperature is fixed, the same for both the upper wall and the lower wall.

3.3 Governing equations

The governing equations are presented for unsteady, incompressible flows, and with constant fluid properties. No heat sources nor sinks are considered and viscous dissipation is neglected. The buoyancy effects are not encompassed, so that the temperature is considered as "passive" within the flow field and subjected to forced convection by the flow.

Dimensionless equations are obtained using the following reference quantities:

- for length, half the average channel height δ
- for velocity, $u^* = (\beta\delta/\rho)^{1/2}$, where β is the constant pressure drop imposed in the streamwise direction x divided by length of the computational domain in streamwise direction L_x:

$$\frac{\overline{P}(x,y,z) - \overline{P}(x+L_x,y,z)}{L_x} = \beta \tag{3.2}$$

- for time, $t^* = \delta/u^*$
- for temperature, the bulk temperature of the channel inlet $T_{b,in}$

Further normalization is performed for the temperature variable in order to obtain a periodic representation of the temperature field, as outlined in section 3.3.2.

3.3.1 Mass and momentum equations

For the simulation of a fully developed flow in a channel, the pressure field P can be expressed as the sum of a linear and an unsteady periodic contributions:

$$P(x, y, z, t) = p(x, y, z, t) - \beta x \tag{3.3}$$

so that periodic boundary conditions can be imposed to the pressure field in the streamwise direction.

The conservation equations for mass and momentum in dimensionless form read as follows:

$$\nabla \cdot \mathbf{u} = 0 \tag{3.4}$$

$$\frac{\partial \mathbf{u}}{\partial t} + \nabla \cdot (\mathbf{u} \otimes \mathbf{u}) = -\nabla p + \frac{1}{\mathrm{Re}^*} \nabla^2 \mathbf{u} + \mathbf{b} \tag{3.5}$$

where $\mathbf{b}$ is the unit vector in x direction, since in the non-dimensional form, $\beta = 1$. The Reynolds number Re^* is defined as $\mathrm{Re}^* = u^* \delta / \nu$. The *friction Reynolds number*, Re_τ is conventionally introduced for numerical simulations of turbulent channel flows, and it is formed using a velocity scale representing only viscous drag effects, $u_\tau = \sqrt{\tau_w / \rho}$. The Reynolds number Re^* has to be distinguished from the Re_τ, as this latter takes into account of both the viscous drag effects and the form drag effects.

3.3.2 Energy equation

Accordingly to our assumptions, the non-dimensional form of the energy conservation equation reads:

$$\frac{\partial T}{\partial t} + \nabla \cdot (\mathbf{u} T) = \frac{1}{\mathrm{Re}^* \mathrm{Pr}} \nabla^2 T \tag{3.6}$$

where the Prandtl number is defined as $\mathrm{Pr} = \nu / \alpha$.

A further normalization of the temperature field is introduced for the direct simulations of the temperature field with

prescribed temperature conditions, by enabling a streamwise periodic variable to be calculated instead of the actual temperature field. The technique used is those proposed by Stalio (2002/2003) for time-dependent fully developed temperature fields with uniform temperature boundary conditions. The technique has been first introduced in the case of ducts with a constant cross section and then extended to the case of ducts having periodic variations of cross-sectional area. The technique is summarized in the following.

Ducts of a constant cross-section

Thermally developed flows in duct with a constant cross section are characterized by the fact that the shape of the temperature profile does not change in the streamwise direction:

$$\frac{\partial}{\partial x}\left(\frac{\overline{T}(x,y)-T_w}{\overline{T}_b(x)-T_w}\right)=0 \tag{3.7}$$

Also, the y-derivative of equation (3.7) at the uniform temperature wall:

$$\frac{\left.\dfrac{\partial \overline{T}}{\partial y}\right|_w}{\overline{T}_b-T_w}=\frac{\overline{h}}{\alpha} \tag{3.8}$$

does not depend on x, which implies, in case of constant flow properties, that the time averaged heat transfer coefficient $\overline{h}$ does not vary with x.

To the condition $\partial\overline{h}/\partial x = 0$ corresponds an exponential decay along x of the temperature difference between the fluid and the solid wall. By neglecting the effects of the streamwise diffusion, an energy balance over the length dx of the plane duct reads:

$$\overline{q}_w \, p \, \mathrm{d}x = \dot{m} \, c \, \mathrm{d}\overline{T}_b \tag{3.9}$$

where $\overline{q}_w (< 0)$ is the heat flux at the wall and p is the wet perimeter, $\dot{m}$ is the mass flow rate and c is the specific heat.

Equation (3.7) can be written also in the form:

$$\frac{\dfrac{\mathrm{d}\overline{T}_b}{\mathrm{d}x}}{\overline{T}_b - T_w} = -\frac{\overline{h} p}{\dot{m} c} \tag{3.10}$$

where the heat transfer coefficient $\overline{h}$ appears. As equation (3.10) does not depend on x, a positive constant Λ can be defined:

$$\Lambda = -\frac{\frac{d}{dx}[\overline{T}_b(x) - T_w]}{[\overline{T}_b(x) - T_w]} \tag{3.11}$$

which represents the exponential temperature decay rate along x, and it can be considered that in a fully developed regime:

$$\overline{T}(x, y) = \overline{T}(x_1, y) \, \mathrm{e}^{-\Lambda (x - x_1)} \tag{3.12}$$

where, for the sake of simplicity, T_w is set to zero. Hence, a normalized temperature θ can be introduced:

$$\theta(x, y, z, t) = \frac{T(x, y, z, t)}{\mathrm{e}^{-\Lambda x}} \tag{3.13}$$

whose averaged value $\overline{\theta}$ does not depend on x, so that for any streamwise length l:

$$\overline{\theta}(0, y, z, t) = \overline{T}(0, y, z, t) = \frac{\overline{T}(l, y, z, t)}{\mathrm{e}^{-\Lambda l}} = \overline{\theta}(l, y, z, t) \tag{3.14}$$

Unlike the temperature T, periodic boundary conditions can be assigned for the normalized temperature θ, and this makes such variable θ more suitable for direct numerical simulations of heat transfer in ducts.

The transport equation of the periodic variable θ is obtained by introducing θ in the energy equation (3.6):

$$\frac{\partial \theta}{\partial t} + \frac{\partial (u_i\,\theta)}{\partial x_i} = \alpha \frac{\partial \theta^2}{\partial x_i^2} + (\alpha\,\Lambda^2 + u\,\Lambda)\,\theta - 2\,\alpha\,\Lambda\,\frac{\partial \theta}{\partial x} \qquad (3.15)$$

From the volume integral of equation (3.15) it results that the ensemble averaged temperature $\overline{\theta}$ increases exponentially in time:

$$\int_V \frac{\partial \overline{\theta}}{\partial t} \mathrm{d}V = \alpha \Lambda^2 \int_V \overline{\theta} \mathrm{d}V \qquad (3.16)$$

and this feature has to be considered when equation (3.15) is numerically solved. A further characteristic is that the variable θ is defined a part from a multiplicative constant C, being C any real constant, included $C = 0$. Hence, if the temperature field θ is a solution of equation (3.15), $C\theta$ satisfies the same equation too. To identify at every integration time-step, dt, the unique physical solution of equation (3.15), an appropriate boundary condition has to be added, in this case that the ensemble averaged bulk temperature $\overline{T}_b$ is constant in time:

$$\int_V \frac{\partial \overline{\theta}}{\partial t} \mathrm{d}V = 0 \qquad (3.17)$$

To calculate the constant temperature $\overline{T}_b$, solution to the equation (3.15), the calculated θ field has to be corrected after each integration time step as follows:

$$\widehat{\theta} = \theta e^{-\alpha \Lambda^2 \mathrm{d}t} \tag{3.18}$$

For the corrected variable $\widehat{\theta}$ results that:

$$\int_V \widehat{\theta}(t) \mathrm{d}V = \int_V \theta(t_0) \mathrm{d}V \tag{3.19}$$

being $\theta(t_0)$ the initial condition field.

Finally, to simulate a fully developed flow and heat transfer in a duct with a constant cross-section and a uniform temperature at wall it is required to calculate the temperature decay rate Λ along the streamwise direction and the solution of the transport equation of the streamwise periodic variable θ.

Extension to periodic ducts

The technique introduced in the previous section is here extended to the case of flows in fully developed conditions in ducts with streamwise periodic variations of the cross sectional area. The assumptions of constant flow properties and prescribed uniform temperature at walls are retained.

An energy balance, which does not take into account of the streamwise diffusion, reads:

$$\overline{q}_w \, p \, \mathrm{d}\xi = \dot{m} \, c \, \mathrm{d}\overline{T}_b \tag{3.20}$$

where $q_w (< 0)$ is the wall heat flux in direction normal to the wall and ξ is the curvilinear coordinate along the solid wall shape. Differently from the case of duct with constant cross-section, in this case the temperature decay rate Λ is not uniform:

$$\Lambda(x) = \frac{\overline{h}(x)\, p}{\dot{m} c \dfrac{\mathrm{d}x}{\mathrm{d}\xi}} \tag{3.21}$$

but for periodic variation of the duct cross-section in the streamwise direction it can be proved that Λ is periodic as well (Patankar et al. 1977), $\Lambda(x) = \Lambda(x + L)$, and if a Λ_L is defined as:

$$\Lambda_L = \frac{1}{L} \int_{x_1}^{x_1+L} \Lambda(x)\, \mathrm{d}x \tag{3.22}$$

then Λ_L is independent of the starting point x_1. By assuming $T_w = 0$ and by considering the definition of Λ, equation (3.21), the energy balance can be also written in this form:

$$\frac{\mathrm{d}\overline{T}_b}{\mathrm{d}x} = -\Lambda\, \overline{T}_b \tag{3.23}$$

whose integration yields:

$$\ln\left(\overline{T}_b(x_2)\right) - \ln\left(\overline{T}_b(x_1)\right) = -\int_{x_1}^{x_2} \Lambda(x)\mathrm{d}x \tag{3.24}$$

and also:

$$\overline{T_b}(x + L) = \overline{T_b}(x)\ \mathrm{e}^{-\Lambda_L L} \tag{3.25}$$

As the ensemble averaged temperature profiles at periodic distances $L, 2L, 3L, \ldots$ are self-similar in this case (Patankar et al. 1977), the equation (3.25) yields also:

$$\overline{T}(x + L, y) = \overline{T}(x, y)\ \mathrm{e}^{-\Lambda_L L} \tag{3.26}$$

Therefore, the normalized temperature can be defined:

$$\theta(x,y,t) = \frac{T(x,y,t)}{\mathrm{e}^{-\Lambda_L\, x}} \tag{3.27}$$

whose ensemble average $\overline{\theta}$ has the property:

$$\overline{\theta}(x,y,t) = \frac{\overline{T}(x,y,t)}{\mathrm{e}^{-\Lambda_L\, x}} = \frac{\overline{T}(x+L,y,t)}{\mathrm{e}^{-\Lambda_L\,(x+L)}} = \overline{\theta}(x+L,y,t) = \ldots \tag{3.28}$$

The normalized temperature variable θ, being periodic in the streamwise direction, can be conveniently used for direct numerical simulations of time-dependent flows in ducts with streamwise periodic geometry and uniform wall temperature. The temperature field T at every time-step can be calculated by solving the equation (3.15) for the normalized temperature θ with the same procedure as for the case of ducts with a constant cross-section.

At each time-step, Λ_L is calculated integrating:

$$\Lambda(x) = \frac{2}{Re_\tau\, Pr}\, \frac{1}{\overline{Q}_s \overline{T}_b}\, \frac{\partial \overline{T}}{\partial \eta} \frac{\partial \xi}{\partial x} \tag{3.29}$$

where Q_s is the specific flow rate and η is the curvilinear coordinate normal to the wall. Differently from the flat channel case, the volume integration of the transport equation for θ is not computed analytically, and the correction of θ to obtain a constant $\overline{T_b}$ solution is provided by evaluating the integral:

$$\int_V \frac{\partial \overline{\theta}}{\partial t} \mathrm{d}V > 0 \tag{3.30}$$

through a running average over a time interval of several large-eddy-turnover-times (LETOT) and then dividing by the latest available value of the integral.

3.4 Non dimensional parameters

Non dimensional, global parameters for the present case-study are the Reynolds number, the friction factor and the Nusselt number:

$$\mathrm{Re} \equiv 2\frac{Q_s}{\nu}; \qquad f \equiv \frac{2(\tau_{w,u}+\tau_{w,l})}{\frac{1}{2}\,\rho\,u_m^2}; \qquad \mathrm{Nu} \equiv \frac{2H_{\mathrm{av}}\,h}{\mathrm{k}} \quad (3.31)$$

where Q_s is the time-averaged volume flow rate per unit spanwise width of the channel, the average velocity is then defined as $u_m \equiv Q_s/H_{\mathrm{av}}$. Wall shear stress of the upper and lower wall $\tau_{w,u}$ and $\tau_{w,l}$ are calculated on the *projected horizontal area*. In the Nusselt number formula $2H_{\mathrm{av}}$ corresponds to the hydraulic diameter.

In the numerical code the Reynolds number Re^* is assigned, while non-dimensional parameters Re, f and Nu are evaluated in terms of non-dimensional quantities by

$$\mathrm{Re} = 2\mathrm{Re}^*\,Q_s; \qquad f = \frac{4\,H_{\mathrm{av}}}{u_m^2\,Re^*}\left\langle\frac{\partial\overline{u}}{\partial y}\right\rangle\Bigg|_w; \quad (3.32)$$

The friction Reynolds number, Re_τ, which does not coincide with Re^* is defined as

$$\mathrm{Re}_\tau = \frac{u_\tau\delta}{\nu}; \qquad u_\tau = \sqrt{\frac{\tau_{w,u}+\tau_{w,l}}{2\rho}} \quad (3.33)$$

The Nusselt number in terms of non dimensional quantities is evaluated from

$$\mathrm{Nu} = \frac{2\,H_{\mathrm{av}}}{\langle T_b\rangle - T_w}\left\langle\frac{\partial\overline{T}}{\partial\eta}\right\rangle\Bigg|_w \quad (3.34)$$

A local Nusselt number can be defined starting from the equation (3.34)

$$\mathrm{Nu}(x) = \frac{2\,H_{\mathrm{av}}}{T_b - T_w}\,\frac{\partial \overline{T}}{\partial \eta}\bigg|_w \tag{3.35}$$

whereas the local $\mathrm{Nu}(x)$ allows for the discussion of heat transfer performance in specific portions of the channel.

Chapter 4

Numerical procedures

This chapter focuses on the numerical methods employed for the solution of the governing equations. The domain discretization and the numerical techniques adopted for DNS simulations are described first. Subsequently, the mesh and the turbulence models used for RANS simulations methods are illustrated.

4.1 DNS simulations

In the present DNSs the instantaneous velocity field $\mathbf{u}$ and temperature field θ are determined by solving equations (3.4), (3.5) and (3.15). The actual temperature field T is then recovered as explained in section 3.3.2. The Reynolds number value $Re = 19\,000$ is simulated, and $Re = 13\,700$ only for validation purposes. The Prandtl number simulated are $Pr = 0.025$, $Pr = 0.2$ and $Pr = 0.71$.

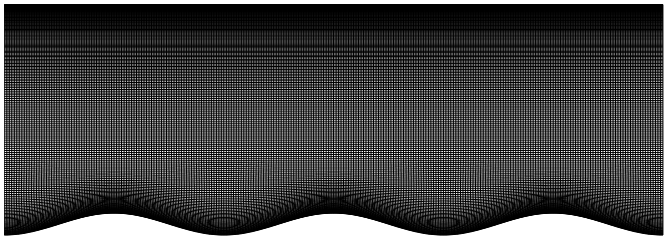

Figure 4.1: The $265 \times 187 \times 221$ computational mesh used for $\mathrm{Re} = 19\,000$, longitudinal view.

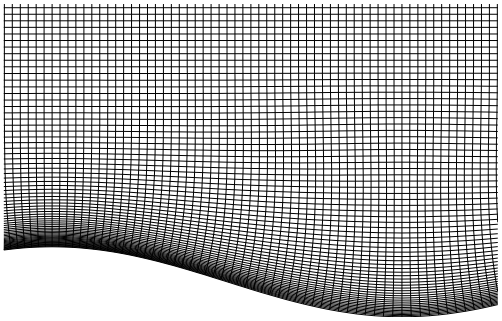

Figure 4.2: Detail of the $265 \times 187 \times 221$ computational mesh used for $\mathrm{Re} = 19\,000$, longitudinal view.

4.1.1 Domain discretization

A structured, curvilinear and orthogonal mesh is employed for the discretization of the 3D computational domain in figure 3.2. The number of grid points set for the calculation at $\mathrm{Re} = 19\,000$ is $265 \times 187 \times 221$ along, respectively, x, y and z. A section of the mesh in the x-y plane is displayed in figure 4.1. A detail of the 265×187 computational mesh in the x-y plane is shown in figure 4.2.

To check the validity of the results obtained, a simulation for $\mathrm{Re} = 13\,700$ has also been performed to match the flow

regime of available published data for the same geometry by Hudson (1993) and by Cherukat et al. (1998). The mesh employed for the validation has $253 \times 129 \times 161$ grid points along x, y and z.

		Re_τ	Δx^+	$\Delta y^+_{\mathrm{mean}}$	y^+_w	$\Delta y^+_{\mathrm{max}}$	Δz^+
Present	$\mathrm{Re} = 19\,000$	282	6.7	3.3	0.53	5.5	7.9
Present	$\mathrm{Re} = 13\,700$	216	5.3	3.6	0.58	5.7	8.3
Maaßet al.(1996)	$\mathrm{Re} = 11\,400$	-	10.2	-	1.6	12.4	10.2

Table 4.1: Grid spacings in wall units.

Grid spacings for the two Reynolds number values simulated are given in Table 4.1, together with the friction Reynolds number values. In the same table some details of the mesh used by Maaßand Schumann (1996) are also reported for comparison.

4.1.2 Numerical method

The Navier-Stokes equations, equations (3.4) and (3.5), and the equation for the variable θ, equation (3.15) with periodic Λ, are solved by a second order projection scheme, as proposed in (Gresho 1990). The numerical integration from the instant $t^{(n)}$ to $t^{(n+1)} = t^{(n)} + \Delta t$ is performed through the following steps:

1. The temperature decay rate $\Lambda_L^{(n)}$ is calculated by the integration of equation (3.29)

2. The new θ field is evaluated:

$$
\begin{aligned}
&\frac{\theta^{(n+1)} - \theta^{(n)}}{\Delta t} = \\
-\ &\frac{1}{2}\left[3\ (\mathbf{u}\cdot\nabla\theta)^{(n)} - (\mathbf{u}\cdot\nabla\theta)^{(n-1)}\right] + \\
+\ &\frac{1}{2\ Re^{*}Pr}\left(\nabla^2\theta^{(n+1)} + \nabla^2\theta^{(n)}\right) + \\
+\ &\frac{1}{2}\left[3\ \sigma(\theta^{(n)}, \Lambda_L^{(n)}) - \sigma(\theta^{(n-1)}, \Lambda_L^{(n-1)})\right]
\end{aligned}
\tag{4.1}
$$

where $\sigma(\theta, \Lambda_L)$ is the source term of the energy equation (3.15)

3. The θ field is corrected to obtain a constant $\overline{T}_b$ solution, as discussed in section 3.3.2

4. The intermediate velocity field $\widetilde{\mathbf{u}}^{(n+1)}$ is determined:

$$
\begin{aligned}
&\frac{\widetilde{\mathbf{u}}^{(n+1)} - \mathbf{u}^{(n)}}{\Delta t} = \\
-\ &\frac{1}{2}\left[3\ (\mathbf{u}\cdot\nabla)\,\mathbf{u}^{(n)} - (\mathbf{u}\cdot\nabla)\,\mathbf{u}^{(n-1)}\right] + \\
+\ &\frac{1}{2\ Re^{*}}\left(\nabla^2\mathbf{u}^{(n+1)} + \nabla^2\mathbf{u}^{(n)}\right) - \nabla p + \mathbf{x}
\end{aligned}
\tag{4.2}
$$

5. The auxiliary variable ϕ is calculated from the Poisson equation:

$$\nabla^2\phi = \nabla\widetilde{\mathbf{u}}^{(n+1)} \tag{4.3}$$

with $\partial\phi/\partial n = 0$ at all wall boundaries, where n is the wall-normal coordinate.

6. The tentative velocity $\widetilde{\mathbf{u}}^{(n+1)}$ is updated, by projection, in order to obtain a divergence free velocity field $\mathbf{u}^{(n+1)}$

from the relation:

$$\mathbf{u}^{(n+1)} = \widetilde{\mathbf{u}}^{(n+1)} - \nabla\phi \tag{4.4}$$

7. The new pressure field is computed at $t^{(n+1)}$ from:

$$p^{(n+1)} = p^{(n)} + \frac{\phi}{2\,\Delta t} \tag{4.5}$$

In equations (4.1) and (4.2), the Crank-Nicolson scheme is used for the temporal discretization of the viscous terms, while the Adams-Bashfort scheme is used for the convective terms and the source term of the energy equation. A finite volume method is used for the integration of the equations (4.1) to (4.3). The spatial discretization is performed by means of second order central difference schemes.

The transport equations are solved with use of an *approximate factorization* method, while the Poisson equation is solved by a fast Poisson solver. Further details can be found in (Stalio 2002/2003).

4.2 RANS simulations

RANS simulations are performed for the Reynolds number value $Re = 19\,000$ and the only Prandtl number value $0\,71$. The two-equations eddy-viscosity turbulence models k-ω SST (Menter 1993) and q-ζ model (Gibson and Dafa'Alla 1995) have been selected for the modeling of the Reynolds stress. The standard gradient-transport model has been used for reproduce the turbulent heat fluxes.
The transport equations of the averaged variables and based on the Boussinesq hypothesis, equation (2.9), read:

$$\frac{\partial \overline{u}_j}{\partial x_j} = 0 \tag{4.6}$$

$$\frac{\partial \overline{u}_j \overline{u}_i}{\partial x_j} = -\frac{1}{\rho}\frac{\partial}{\partial x_i}\left(\overline{P} + \frac{2}{3}\rho k\right) + \frac{\partial}{\partial x_j}\left[(\nu + \nu_t)\frac{\partial \overline{u}_i}{\partial x_j}\right] \tag{4.7}$$

$$\frac{\partial \overline{u}_j \overline{T}}{\partial x_j} = \frac{\partial}{\partial x_j}\left(\alpha \frac{\partial \overline{T}}{\partial x_j} - \overline{u_j' T'}\right) \tag{4.8}$$

4.2.1 Domain discretization

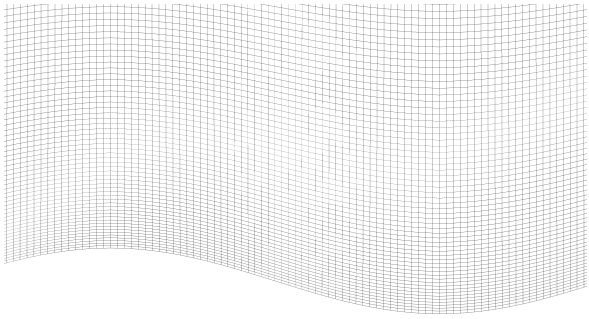

Figure 4.3: Detail of the 288×128 computational mesh.

The mesh used for the discretization of the 2D-domain, figure 3.3, is structured, non-orthogonal, with 288×128 grid points along x and y. The mesh nodes are uniformly distributed along x, and like as a "bell-curve" along y. The first node from the wall is located on average at a $y^+ = 1.17$. This grid refinement has been adopted to use the q-ζ model without resorting to the wall functions, thus to optimize the model performance. A detail of the mesh is shown in figure 4.3.

4.2.2 Numerical methods

The two-equations eddy-viscosity turbulence models k-ω SST and q-ζ have been selected for their favorable characteristics into treat flows with the alternating occurrence of adverse and favorable pressure gradients, as it occurs in the present case study. In particular, the k-ω SST model (Menter 1993) is renown for a good behavior with separated flows, and the q-ζ model (Gibson and Dafa'Alla 1995) is particularly suited for the modeling of separating flows, and also it has the favorable characteristic that both model variables ($q = \sqrt{k}$ and its dissipation rate ζ) are zero at the wall and are well behaved, in that they vary linearly with the distance from the wall for small y, thus not requiring the use of the wall-functions "to bridge" the viscous near-wall region.

The Simple Gradient Diffusion Hypothesis (SGDH) is used to reproduce the turbulent heat fluxes, as it is the most largely used in the common practice and a very simple model.

The k-ω SST model

The Shear-Stress Transport k-ω model was developed by Menter in 1993 to combine the accuracy of the k-ω model in the near-wall region with the free-stream independence of the k-ϵ model in the far field. This is obtained by multiplying both the formulation of the standard k-ω model and k-ϵ model by a "blending function" and then to add together the two formulations. The blending function is designed to be one in the near-wall region, which activates the k-ω model, and zero far from the surface, which activates the k-ϵ model. The definition of the turbulent eddy-viscosity, ν_t, accounts for the transport of the turbulent shear-stress, the reason why the

model is called Shear-Stress Transport k-ω model.

The transport equations of the turbulent scalar variables k and ω read:

$$\frac{Dk}{Dt} = \frac{\partial}{\partial x_j}\left[(\nu + \sigma_k \nu_t)\frac{\partial k}{\partial x_j}\right] + G_k - Y_k \tag{4.9}$$

$$\frac{D\omega}{Dt} = \frac{\partial}{\partial x_j}\left[(\nu + \sigma_\omega \nu_t)\frac{\partial \omega}{\partial x_j}\right] + G_\omega - Y_\omega + D_\omega \tag{4.10}$$

being σ_k and σ_ω model constants.

In the transport equation of k the term G_k represents the generation of turbulent kinetic energy, Y_k instead represents the dissipation of turbulent kinetic energy, and they are calculated as:

$$G_k = -\overline{u_i' u_j'}\frac{\partial u_j}{\partial x_i} \tag{4.11}$$

$$Y_k = \beta^* \omega k \tag{4.12}$$

where β^* is a constant.

In the transport equation of ω, the terms G_ω, Y_ω and D_ω represent, respectively, the generation term, the dissipation term and the cross-diffusion term. They are calculated as follows

$$G_\omega = -\frac{\gamma}{\mu_t}\overline{u_i' u_j'}\frac{\partial u_j}{\partial x_i} \tag{4.13}$$

$$Y_\omega = \beta \omega^2 \tag{4.14}$$

$$D_\omega = 2(1-F_1)\sigma_{\omega 2}\frac{1}{\omega}\frac{\partial k}{\partial x_j}\frac{\partial \omega}{\partial x_j} \tag{4.15}$$

being γ, β, and σ_{ω_2} model constants and F_1 the blending function. The eddy-viscosity ν_t is determined following this expression:

$$\nu_t = \frac{a_1 k}{max(a_1\omega;\Omega)} \tag{4.16}$$

where $\Omega = \partial\overline{u}/\partial y$. The above expression guarantees that in the regions of adverse pressure gradients, where the production of turbulent kinetic energy is greater than dissipation (or $\Omega > a_1\omega$), the ν_t is determined as

$$\nu_t = \frac{a_1 k}{\Omega} \tag{4.17}$$

and that for the rest of the boundary layer, where this latter expression leads to infinitely high eddy-viscosity at points where Ω goes to zero, ν_t is calculated as

$$\nu_t = \frac{a_1 k}{a_1\omega} \tag{4.18}$$

For the complete formulation of the model see (Menter 1993).

The model has been employed by means of the CFD package OpenFOAM 2.0.1, where a first order spatial scheme has been used. The behavior of the model variables in the viscous sublayer has been modeled by the use of wall-functions.

The q-ζ model

For the modeling of the Reynolds stress the q-ζ model solves extra transport equations for q, the square-root of turbulent kinetic energy $q = \sqrt{k}$, and ζ, the dissipation rate of q, $\zeta = \tilde{\epsilon}/2q$, where $\tilde{\epsilon}$ is the isotropic dissipation rate. As mentioned above, the main characteristic of this model is that both its variables, q and ζ, are zero at the walls and vary linearly with the distance from the wall for small y. The use of wall-functions, which should be highly restrictive, especially when separated flow regions or recirculation regions occur, is not required in this case.

The equations for the model variables are:

$$\frac{Dq}{Dt} = \frac{\partial}{\partial x_j}\left[(\nu + \frac{\nu_t}{\sigma_q})\frac{\partial q}{\partial x_j}\right] + Q - \zeta \tag{4.19}$$

$$\frac{D\zeta}{Dt} = \frac{\partial}{\partial x_j}\left[(\nu + \sigma_\zeta \nu_t)\frac{\partial \zeta}{\partial x_j}\right] + \frac{\zeta}{q}(C_{\zeta 1} f_{\zeta 1} Q - C_{\zeta 2} f_{\zeta 2}\zeta) + \Psi \tag{4.20}$$

where Q is the rate of production of q:

$$Q = \gamma_1 \frac{\partial u_i}{\partial x_j}\left(\frac{\partial u_i}{\partial x_j} + \frac{\partial u_j}{\partial x_i}\right) \tag{4.21}$$

and

$$\Psi = 2\nu\gamma_t \left(\frac{\partial^2 u_i}{\partial x_k \partial x_m}\right)\left(\frac{\partial^2 u_i}{\partial x_k \partial x_m}\right) \tag{4.22}$$

$$\gamma_t = \frac{C_\mu f_\mu}{4}\frac{q^2}{\zeta} \tag{4.23}$$

and where $C_{\zeta 1}$, $C_{\zeta 2}$ and C_μ are model constants and $f_{\zeta 1}$, $f_{\zeta 2}$ and f_μ are damping functions.

The eddy-viscosity is:

$$\nu_t = 2q\gamma_t \tag{4.24}$$

The model constants are the same of the standard k-ϵ model, while the damping functions are different accounting also for the viscous effects in the near-wall region. The complete formulation and the constants values are reported in (Gibson and Dafa'Alla 1995).

Simulations have been performed by use of OpenFOAM 2.0.1, where a first order solver has been used.

The standard gradient-transport model

On the base of the standard gradient-transport model, discussed in section 2.2, the turbulent scalar fluxes are modeled as follows:

$$\overline{u_i' T'} = -\frac{\nu_t}{Pr_t}\frac{\partial \overline{T}}{\partial x_i} \tag{4.25}$$

where the ratio ν_t/Pr_t represents the eddy-diffusivity, α_t. Pr_t is the turbulent Prandtl number, to be set uniform. As mentioned in chapter 2, such an approach is very simple and numerically robust, however, by considering an isotropic eddy-diffusivity, it fails to represent the local dependence of the heat flux on the Reynolds stress and the mean shear. Also, it poses the problem of selecting a suitable value for the uniform turbulent Prandtl number, while it depends on the molecular

Prandtl number value, on the geometry of the problem and flow regime. For the present RANS simulations the turbulent Prandtl number has been fixed equal to 0.85. As revealed by DNS results the assumption of a uniform distribution of Pr_t is not verified in the present case study (section 6.2), however the mean value of turbulent Prandtl number results quite close to 0.85, which is the value conventionally assigned to Pr_t in case of a molecular Prandtl number of order unity. The turbulent heat fluxes distribution, as predicted by the SGDH approach, is moreover strictly influenced by the turbulence model adopted for the eddy-viscosity ν_t. These features will be also recalled in the analysis of the results.

Chapter 5

Validation of DNS method

This chapter includes the validation study performed for the present DNS method.

For the validation study DNS simulations have been performed for a Reynolds number value 13 700, which is comparable with those of the reference data, the experiments by Hudson (1993) and DNS data by Cherukat et al. (1998). Reference data, available for the velocity field, have been taken directly from figures shown in (Cherukat et al. 1998), in particular Figures (10a), (10b), (11a) and (11b). These figures display the profiles of the mean velocity components and the profiles of the root-mean-square fluctuating velocity components.

The Reynolds number based on the mean velocity and the hydraulic diameter of the present simulation $\mathrm{Re} = 13\,700$ does not match exactly the Reynolds number of reference data, $\mathrm{Re} = 13\,840$ becouse in the numerical methodology employed, where the flow is pressure driven, the average velocity is a re-

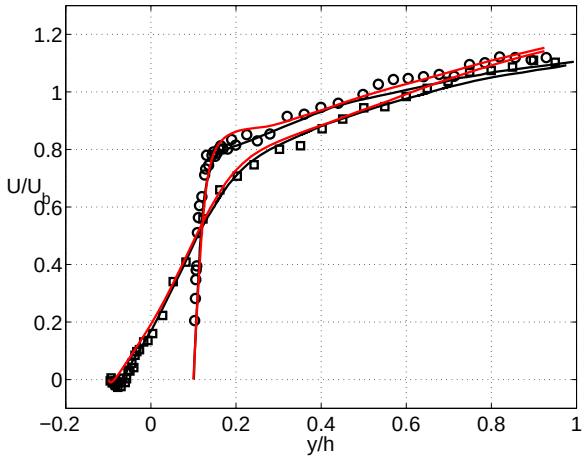

Figure 5.1: Profiles of the mean streamwise velocity component normalised by the bulk velocity for crest and trough. Red lines indicate present results; symbols indicate measurements by Hudson (1993); black lines are for the DNS by Cherukat et al. (1998).

sult of the simulations.

	x_s/λ	x_r/λ
Present	0.14	0.57
(Cherukat et al. 1998)	0.14	0.59

Table 5.1: Separation and reattachment positions of the mean flow, comparison between DNS results.

Flow separation occurs for the selected flow regime, and a mean recirculation bubble is found extending from past the crest of the wave to past the trough. Flow separation and reattachment locations are indicated in table 5.1, where they

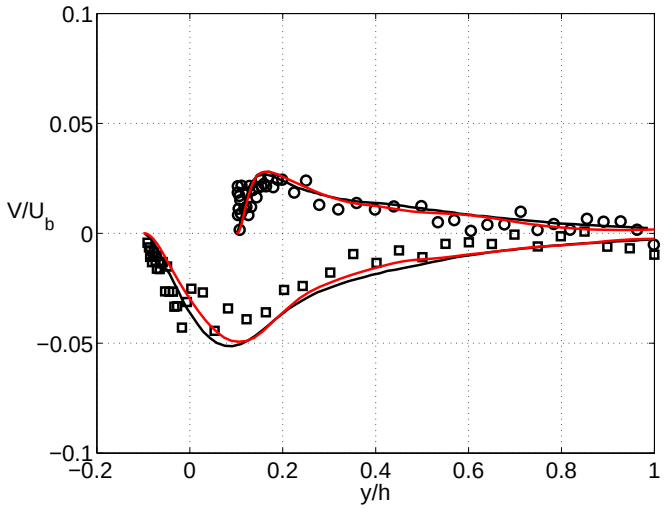

Figure 5.2: Profiles of the mean vertical velocity component normalised by the bulk velocity for crest and trough. Red lines indicate present results; symbols indicate measurements by Hudson (1993); black lines are for the DNS by Cherukat et al. (1998).

are successfully compared to the results by Cherukat et al. (1998).

Figures from 5.1 to 5.4 display the comparison between current results and reference data. Profiles of the main averaged quantities and first order moments are seen to be quite well represented by the present simulations, when compared to both experiments and previous numerical simulations.

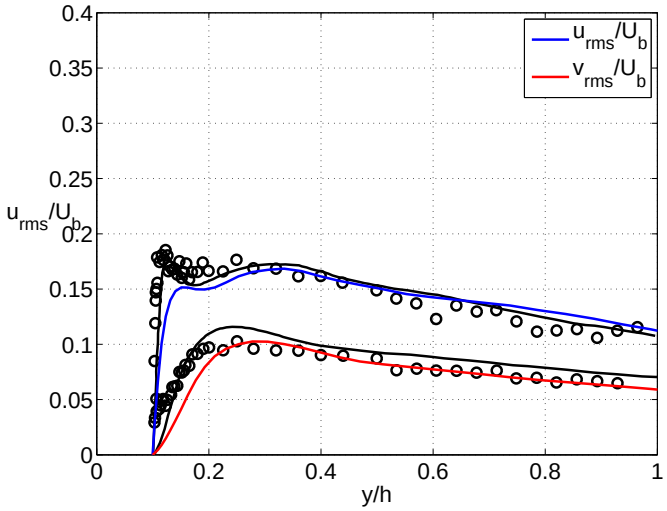

Figure 5.3: Profiles of the root-mean-square of the fluctuating velocity component normalised by the bulk velocity for crest. Symbols indicate measurements by Hudson (1993); black lines are for the DNS by Cherukat et al. (1998).

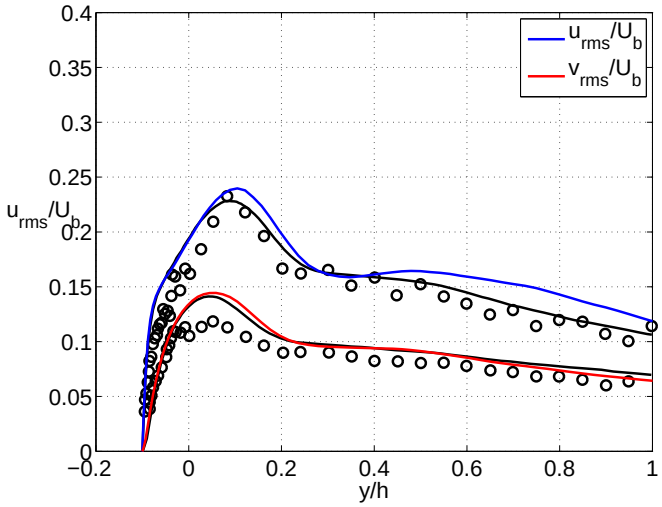

Figure 5.4: Profiles of the root-mean-square of the fluctuating velocity component normalised by the bulk velocity for trough. Symbols indicate measurements by Hudson (1993); black lines are for the DNS by Cherukat et al. (1998).

Chapter 6

Results of DNS simulations

The results obtained by DNS simulations at $\mathrm{Re} = 19\,000$ are presented in this chapter. Three different temperature fields are encompassed, for $\mathrm{Pr} = 0.025$, 0.20 and 0.71. The results for both the velocity and the temperature fields are provided in terms of the non-dimensional variables, as defined in section 3.3.

The main focus is on the flow separation effects and Prandtl number effects on the turbulent heat transport mechanisms. Further, the accuracy of three selected turbulence diffusion models is assessed against the DNS predictions of turbulent heat fluxes, with comments on the accuracy of the selected models in case of separated flow conditions and non unity Prandtl number fluids.

After a statistically steady state is reached, fluid flow and thermal field realizations are saved every 0.05 non-dimensional time units and for a period of 12.5 flow-through times, in

order to form statistics. The mean quantities besides being integrated in time are also averaged over the three waves and the spanwise length L_z.

6.1 Velocity field

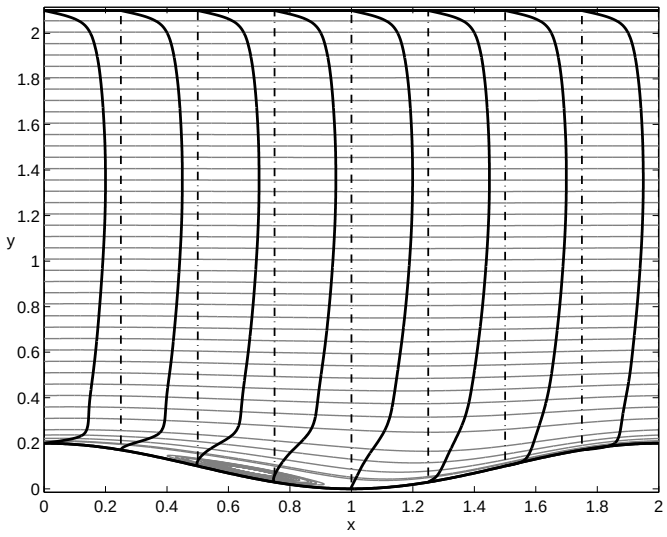

Figure 6.1: Profiles of the streamwise component of the time-averaged velocity field and streamlines.

Streamlines of the averaged velocity field on the periodic module of the channel are depicted in figure 6.1, together with profiles of the streamwise component of velocity. Closer streamlines over the crest of the waves indicate flow acceleration; past the crest, the adverse pressure gradient encountered induces flow separation. The separation and reattachment locations are detected, respectively, at $x_s = 0.28$ and $x_r = 1.1$.

The thickening of the boundary layer before separation is evident from profiles of $\overline{u}$; also the steep velocity gradient at the restart of the boundary layer can be observed. Peak velocity profiles are located well above $y = 1$, *i.e.* above half the averaged channel height, this indicates that the lower wall undulation has a non-negligible influence on the turbulent flow features across the whole channel.

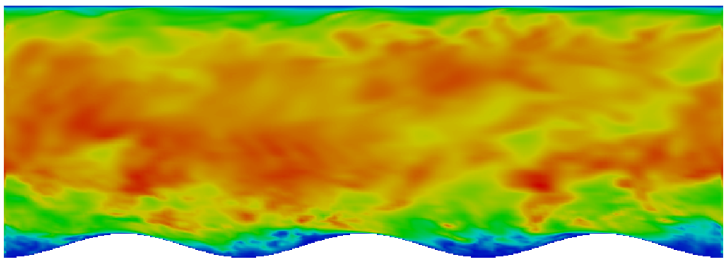

Figure 6.2: Longitudinal view of the instantaneous velocity field for $\mathrm{Re} = 19\,000$ at $z = 3$. Red and blue colors correspond to higher and lower velocity respectively.

A longitudinal view of the instantaneous velocity field is shown in figure 6.2. A cross-sectional view of the instantaneous velocity field is instead reported in figure 6.3 for different streamwise position, $x = 3.2$ which corresponds to the attached mean flow upstream the separation point, $x = 4$ which is in the mean recirculation region, and $x = 4.3$ which corresponds to the restart of boundary layer of the mean flow. A very different behavior is observed in the region close to the wavy wall as the streamwise position varies from $x = 3.2$ to the subsequent $x = 4$ and $x = 4.3$. It can be inferred that much more intense fluctuations occur in correspondence of the mean flow recirculation region and the restarting bound-

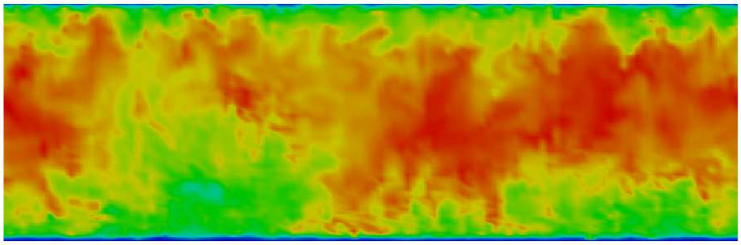

(a) $x = 3.2$

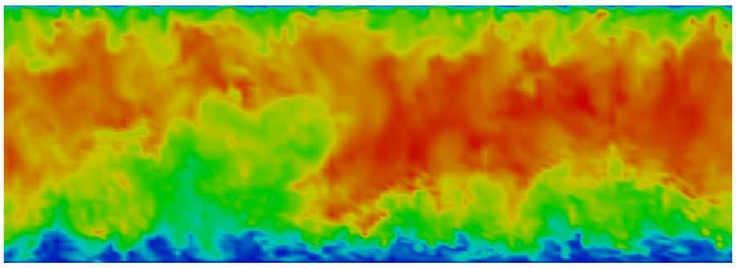

(b) $x = 4$

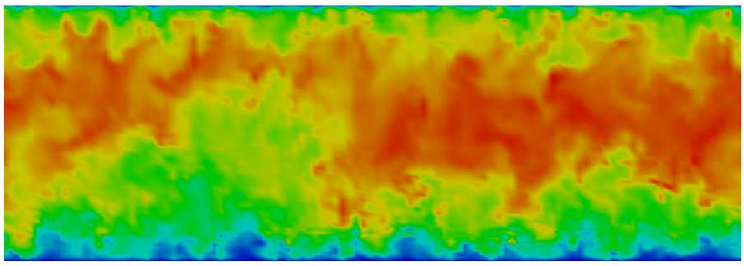

(c) $x = 4.3$

Figure 6.3: Cross-sectional view of the instantaneous velocity field for Re = 19 000. Red and blue colors correspond to to higher and lower velocity respectively.

ary layer region, with respect to the region close to the crest of the wave, where the flow is fully attached to the wall. This also confirms the beneficial effects of flow separation and reat-

tachment on the turbulent mixing.

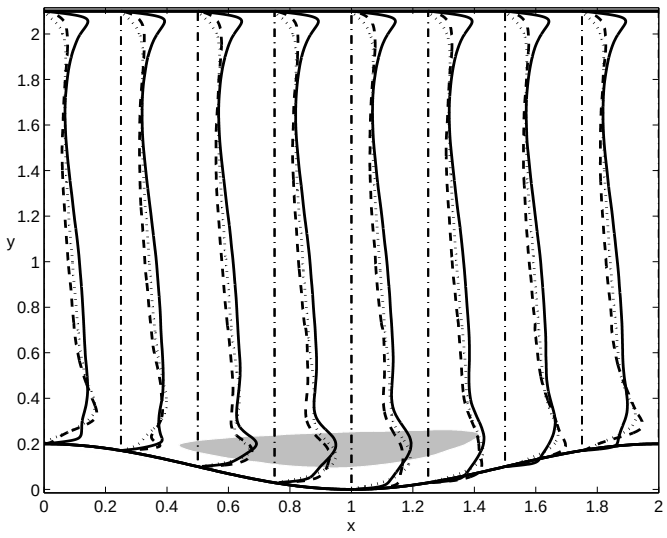

Figure 6.4: Profiles of the root-mean-square velocity fluctuations. Solid line, u'_{rms}; dotted line, v'_{rms}; dashed line, w'_{rms}. The grey area is the region where Reynolds stress $-\overline{u'v'}$ are greater than 2.1.

Figure 6.4 shows the root-mean-square fluctuation profiles for all three components of the velocity; root-mean-square profiles undergo significant modifications for different axial positions. The region with peak velocity fluctuations is located above the trough, correspondent to the shear layer which separates from the crest of the wave and develops downstream. The grey area in figure 6.4 represent the shear layer region where Reynolds stress are the most intense, in particular they locally exceed the threshold $-\overline{u'v'} \geq 2.1$.
Reynolds stress profiles are drawn in figure 6.5. In the lower portion of channel the profiles of Reynolds stress exhibit two

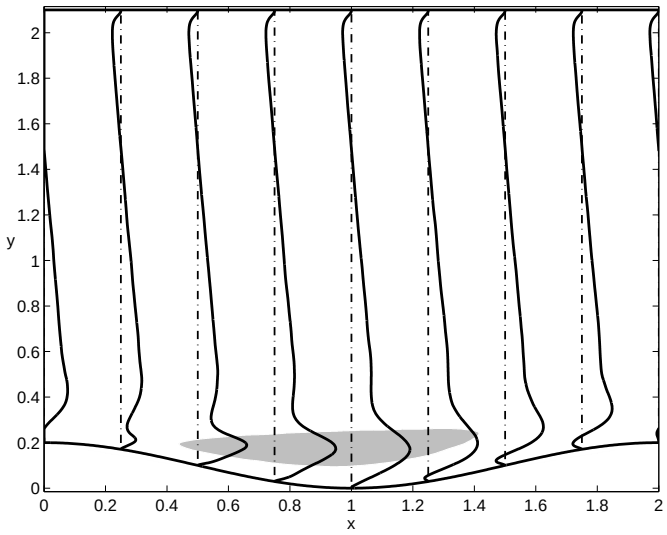

Figure 6.5: Profiles of the Reynolds stress $-\overline{u'v'}$. The grey area is the region where Reynolds stress $-\overline{u'v'}$ are greater than 2.1, while in the whole field $-0.50 < -\overline{u'v'} < 3.13$.

different peaks where attached flow condition subsists, *i.e.* $x < x_s$ and $x > x_r$: the peak in the near-wall region, and the peak which falls in the separated shear layer. On the up-slope portion of the wave the peak values in the near-wall region are negative. This means that also the derivative in y direction of the turbulent shear stress is locally negative, making the turbulent flux of momentum in vertical direction oppose to the momentum flux of viscous origin.

A quadrant-hole analysis is also conducted to investigate on the events contributing to the production of Reynolds stress. In quadrant-hole analysis, firstly introduced by Lu and Willmarth (1973), velocity fluctuations are conditionally sampled to determine the relative contribution of four quadrants –

corresponding to four different types of event– to the formation of statistics. At any point of a statistically steady flow, the contribution from quadrant k ($k = 1, \ldots, 4$) to the Reynolds stress with threshold level (hole size) h is given by

$$\phi^k_{RS}(h) = \frac{\overline{(u'v')^k}}{\overline{u'v'}} D^k_{RS}(h) \tag{6.1}$$

where the average $\overline{(u'v')^k}$ is restricted to data belonging to quadrant k, and $D^k_{RS}(h)$ is the *duration fraction* of the Reynolds stress in quadrant k for which the threshold level h is satisfied

$$D^k_{RS}(h) = \frac{1}{N} \sum_{j=1}^{N} I^k_j(h) \tag{6.2}$$

The indicator function $I^k_j(h) = 1$ if (u', v') is in the k-th quadrant and $|u'v'| \geq h \left|\overline{u'v'}\right|$ in the same location, while $I^k_j(h) = 0$ otherwise.

Quadrant-hole analysis of the Reynolds stress has been performed for subsequent axial positions and two different vertical distances from the wall $y^+ = 10$ and $y^+ = 50$. Quadrant analysis has also been performed on the upper wall of the wavy channel at the same distances $y^+ = 10$ and $y^+ = 50$ from the solid wall and streamwise locations. Results obtained at the upper wall do not depend on x. Accordingly, the contribution $\phi^k_{RS}(h)$ calculated on the upper flat wall is herein referred to as reference data and are used for comparison in the following discussion. As shown in figure 6.6, sweep events are seen to provide the largest contribution to the production of Reynolds stress for axial coordinates $x = 0.1$ to $x = 1.0$, also ejections are seen to contribute significantly. This can be set in relation with the presence of well identified streamwise vortices. The inception of streamwise vortices in the

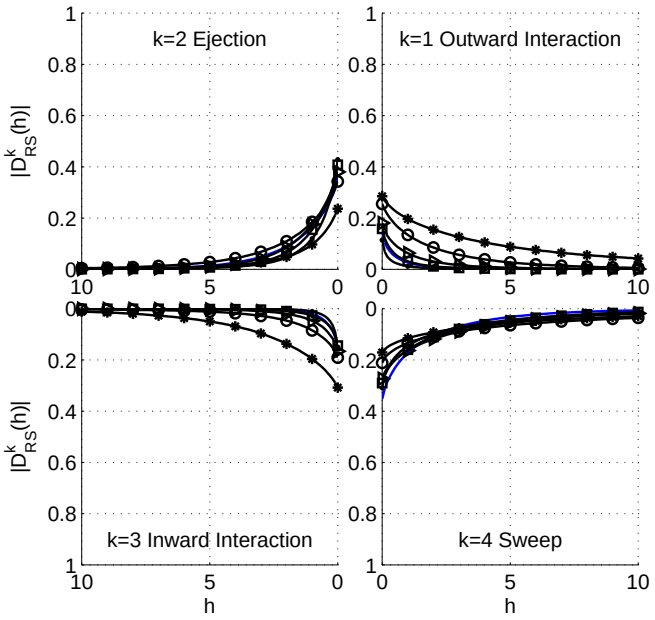

Figure 6.6: Quadrant-hole analysis of Reynolds stress for subsequent axial positions at $y^+ = 10$. Circles correspond to $x = 0.1$, dots to $x = 0.3$ squares to $x = 0.5$, triangles to $x = 1.0$ and asterisks to $x = 1.5$. Solid blue lines indicate reference data.

up-slope region and their projection over the trough before their "loss of identity" was already observed by Calhoun and Street (2001). For $x = 1.5$, sweeps, $k = 1$ and $k = 3$ events of very large intensity with respect to the mean concur with opposite sign to form the local Reynolds stress value. The outward interaction is the largest contribution; this is in direct relation with the negative value for $-\overline{u'v'}$ in the near-wall region about $x = 1.5$, see figure 6.5. At a larger distance from the wall and for example at the $y^+ = 50$ of our calculations,

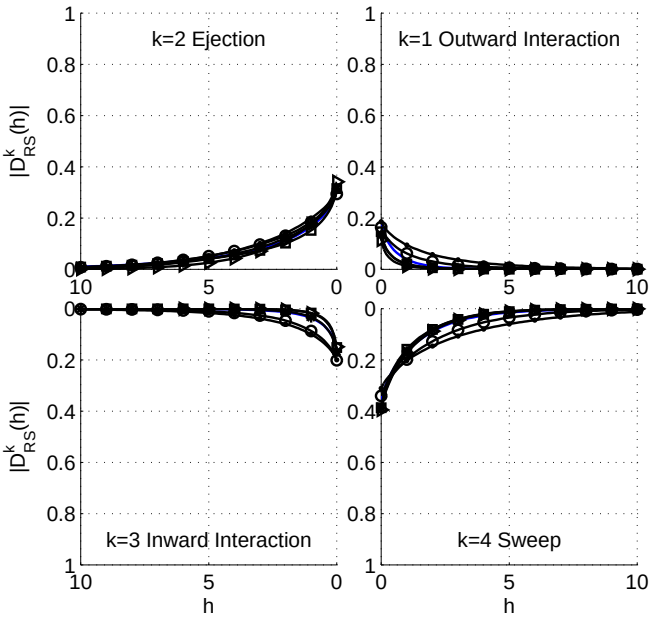

Figure 6.7: Quadrant-hole analysis of Reynolds stress for subsequent axial positions at $y^+ = 50$. Circles correspond to $x = 0.1$, dots to $x = 0.3$ squares to $x = 0.5$, triangles to $x = 1.0$ and asterisks to $x = 1.5$. Solid blue lines indicate reference data.

quadrant analysis results are more similar to the reference data, see figure 6.7.

Friction factor

Friction factor values calculated as in equation (3.32) are reported in Table 6.1 together with reference values for the flat channel from the literature. Due to the presence of a separation bubble, viscous drag on the wavy wall is smaller than that calculated on the upper flat wall. Friction on the upper

	flat channel Eq. (6.3)	flat channel (Moser et al. 1999)	flat wall Present	wavy wall Present
$\mathrm{Re} = 19\,000$	0.0249	-	0.0345	0.0247
$\mathrm{Re} = 11\,172$	0.0338	0.0324	-	-
$\mathrm{Re} = 24\,405$	0.0278	0.0260	-	-

Table 6.1: Friction factor values in the wavy channel for the flat wall and the wavy wall. Flat channel results are reported for comparison; DNS data at $\mathrm{Re} = 11\,172$ ($\mathrm{Re}_\tau = 180$) and $\mathrm{Re} = 28\,405$ ($\mathrm{Re}_\tau = 395$) are taken from (Moser at al. 1999); the empirical relation by Dean is given in (Dean 1978).

wall is instead larger than the value given for a flat channel case at the same Re and calculated by an empirical relation devised by Dean (1978).

$$f = 0.292\ \mathrm{Re}^{-1/4} \tag{6.3}$$

The closest available published data from flat channel DNSs are also reported in Table 6.1. The relation by Dean provides values which exceed the DNS data. The fact that the friction factor on the flat wall of the wavy channel is higher with respect to those predicted by Dean relation for flat channel case clearly indicates that the undulation of the lower wall increases the flat wall drag.

6.2 Temperature field

In order to make the temperature fields calculated for the Prandtl number $\mathrm{Pr} = 0.025$, 0.20 and 0.71 comparable, they have been scaled. As the θ-field is defined a part from a

multiplicative constant, equation (3.13), the scaling has been performed as follows:

$$\theta_s = \theta \cdot \mathrm{Re}_\tau \mathrm{Pr} \left(\left\langle \frac{\partial \overline{\theta}}{\partial y} \right\rangle \Big|_{w,u} \right)^{-1} \tag{6.4}$$

The selected multiplicative constant also makes the temperature distribution in the flat wall region comparable to those of the flat channel case for isoflux BCs at walls ($q_w = \mathrm{Re}_\tau \mathrm{Pr}$), that is convenient for the discussion of results.

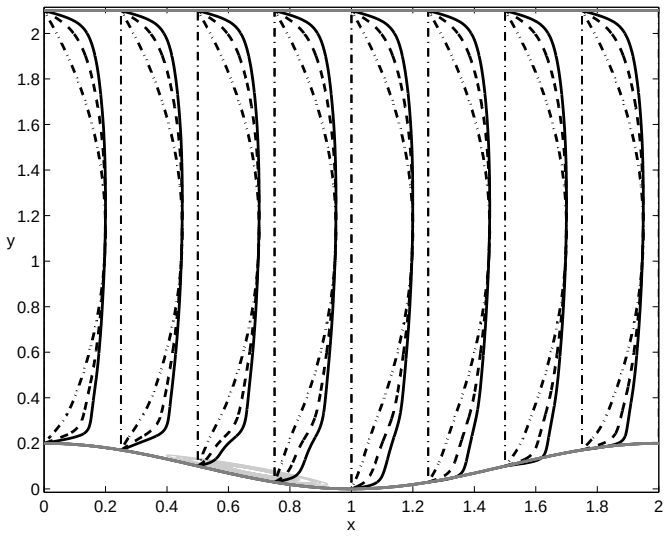

Figure 6.8: Profiles of the averaged thermal field $\overline{\theta_s}$ together with the mean recirculation bubble. Solid lines correspond to Pr = 0.71, dashed lines to Pr = 0.20, dash-dot lines to Pr = 0.025.

Profiles of the averaged temperature field $\overline{\theta_s}$ are represented in figure 6.8. As can be noticed, the temperature distributions depend strongly on the Prandtl number investi-

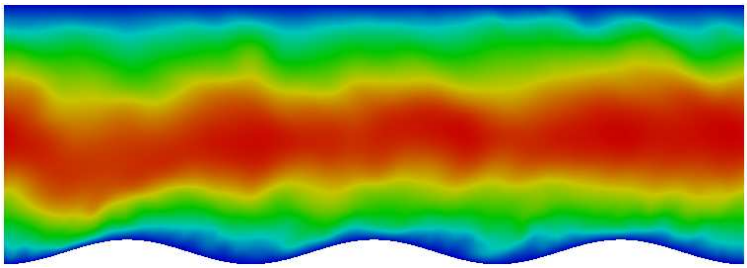

(a) Pr = 0.025

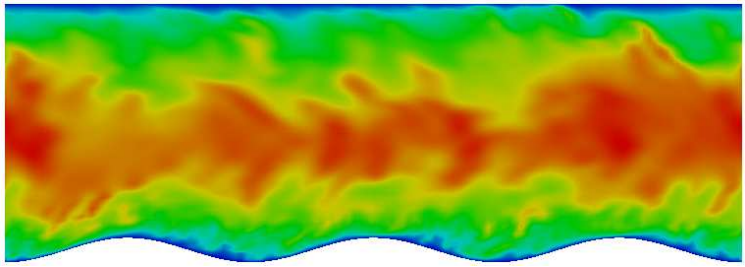

(b) Pr = 0.20

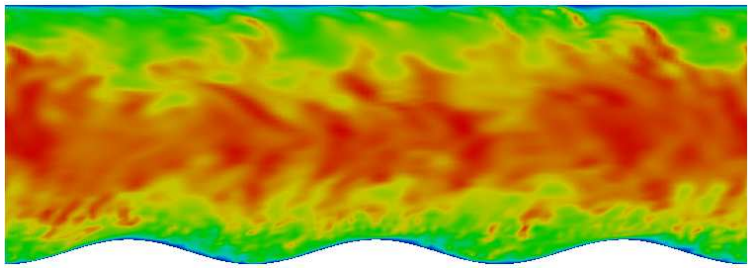

(c) Pr = 0.71

Figure 6.9: Longitudinal view of the instantaneous temperature fields for Re = 19 000. Red and blue colors correspond to higher and lower temperature respectively.

gated. A typical turbulent shape is observed in the Pr = 0.71 case, while a laminar profile corresponds to Pr = 0.025, al-

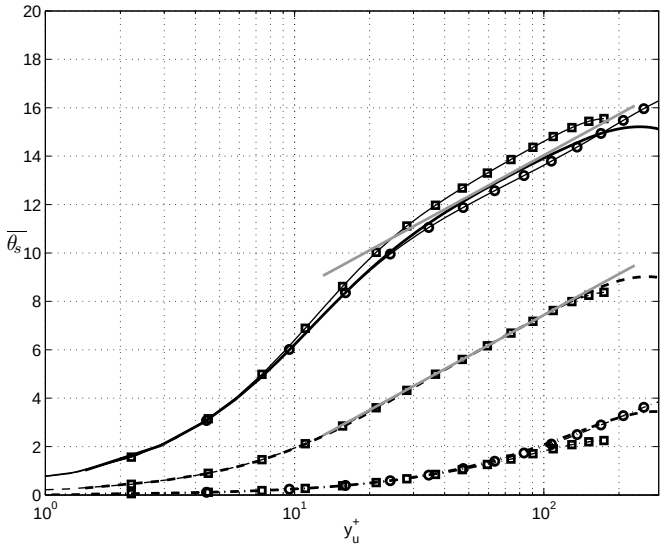

Figure 6.10: x-Averaged temperature profile. Solid black line corresponds to Pr = 0.71, dashed lines to Pr = 0.20, dash-dot line to Pr = 0.025. The grey solid lines correspond to the log-law for the thermal field. Symbols correspond to DNS data by $\mathrm{Re}_\tau = 180$ and circles for $\mathrm{Re}_\tau = 395$.

though the velocity field is the same. The temperature distribution calculated for Pr = 0.20 follows more closely results for Pr = 0.71.

From the maps of the instantaneous temperature fields, drawn in figure 6.9, it can be seen that, as opposite to the Pr = 0.025 case, for Pr = 0.20 and Pr = 0.71 the smaller eddies are very different from the largest one, as much by increasing the Prandtl number. In these cases it results that the Prandtl number effects on the passive scalar field is similar to the Reynolds number effects in dynamics of turbulence, where the difference between the largest eddies and the smallest one

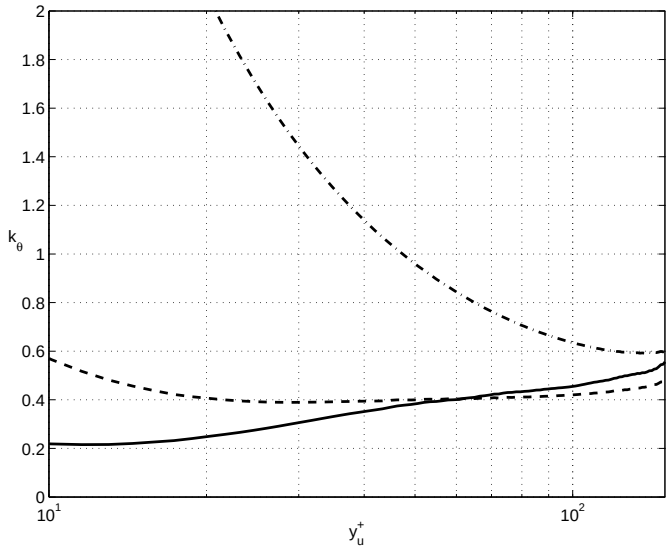

Figure 6.11: k_θ as function of the wall-normal distance from the flat wall. Solid black line corresponds to Pr = 0.71, dashed lines to Pr = 0.20, dash-dot lines to Pr = 0.025.

as scale increases with increasing Reynolds number.

With reference to figure 6.8 it can be seen that in the region close to the upper wall the mean temperature variation in the streamwise direction are small, the maximum relative variation $(\overline{\theta_{s,max}} - \overline{\theta_{s,min}})/T_b = 0.0038$, for a distance from the upper wall which is in terms of friction units $y_u^+ = 79$. The x-averaged $\theta_s(y_u^+)$ profile is represented in figure 6.10, together with the DNS results by Kawamura et al. (1998) for the flat channel case. As opposed to Pr = 0.71 and Pr = 0.20 cases, for Pr = 0.025 a logarithmic region in the mean temperature profile can not be distinguished. In figure 6.10 the straight grey lines represent the log-law for the thermal field (Kader and Yaglom 1972):

$$\overline{\theta_s}^{+}(y_u^+) = \frac{1}{k_\theta}\log(y_u^+) + c_\theta \tag{6.5}$$

The straight lines are drawn only for the values of the Prandtl number 0.20 and 0.71, since a constant slope for the logarithmic profile ($1/k_\theta$) can not be obtained for Pr = 0.025, as shown in the following. Coefficients k_θ and c_θ of equation (6.5) have been calculated by using the present DNS data in the relationships:

$$k_\theta(y_u^+) = \frac{1}{y_u^+}\left(\left\langle \frac{d\overline{\theta_s}^{+}}{dy_u^+} \right\rangle\right)^{-1} \tag{6.6}$$

$$c_\theta(y_u^+) = \overline{\theta_s}^{+} - \frac{1}{k_{\theta_s}}\log(y_u^+) \tag{6.7}$$

being the equation (6.6) obtained by the y-derivative of (6.5), and the equation (6.7) correspondent to the equation (6.5) explicit for c_θ. The profile of $k_\theta(y_u^+)$ is represented in figure 6.11. An almost constant behavior is observed for Pr = 0.20 and Pr = 0.71 and for $50 < y_u^+ < 100$, where k_θ results equal to 0.41, very close to the value found by Kawamura et al. (1999) in channel flow ($k_\theta = 0.4$). The profile of $c_{\theta_s}(y_u^+)$, which is not represented here for sake of brevity, also shows a plateau, where $c_\theta = -3.8$ for Pr = 0.20 and $c_\theta = 2.9$ for Pr = 0.71.

The profiles of the root-mean-square of temperature fluctuations are depicted in figure 6.12 for different axial positions. For Pr=0.025 case the temperature fluctuations are less intense and the shape of the profiles does not correspond to a turbulent temperature field, coherently with the laminar profiles of the correspondent averaged thermal field. Differently from the flat channel case minima $\theta'_{s,rms}$ are observed

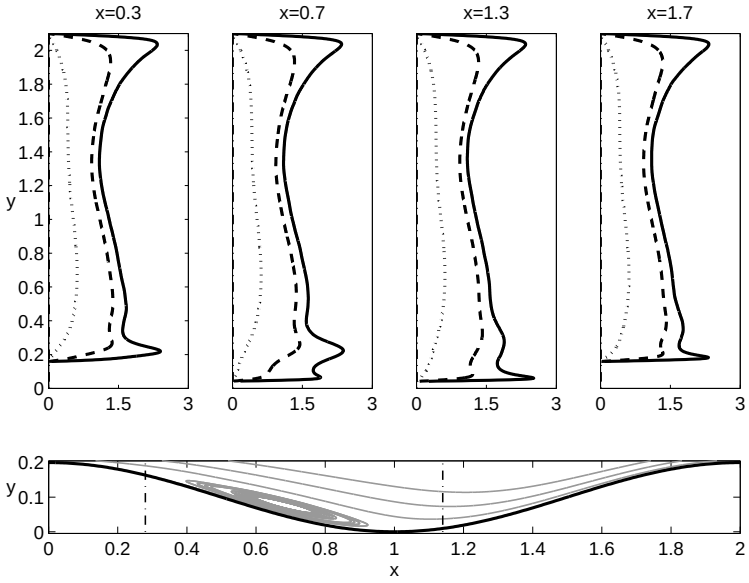

Figure 6.12: Profiles of $\theta'_{s,rms}$. Solid lines are for Pr = 0.71, dashed lines are for Pr = 0.20, dotted lines are for Pr = 0.025. Dash-dot lines in the bottom inset indicate the separation and reattachment locations.

beyond the half channel height, at $y = 1.4$, this indicates that the influence of the lower wall shape is also felt beyond the half channel height. At the upper wall the profiles do not vary with the streamwise coordinate, and peaks of temperature fluctuations are observed at $y_u^+ = 15$ for Pr=0.71 and further from the wall, at $y_u^+ = 29$ for Pr=0.20, consistently with the thicker conductive layer of the averaged temperature field in the latter case. Close to the wavy wall the shape of the profiles significantly changes along x. For the streamwise location within the recirculation region, *i.e* $x = 0.7$, double peaks appear, the peak closer to the wall corresponds to the

top boundary of the mean bubble, while the other one corresponds to the separated shear layer. In the up-slope portion of the wave, *i.e.* $x = 1.3$ and *i.e.* $x = 1.7$, where strong temperature gradients occur in the near wall region, a sharper peak of $\theta'_{s,rms}$ is found close to the wall, while the peak correspondent to the separated shear layer seems considerably reduced.

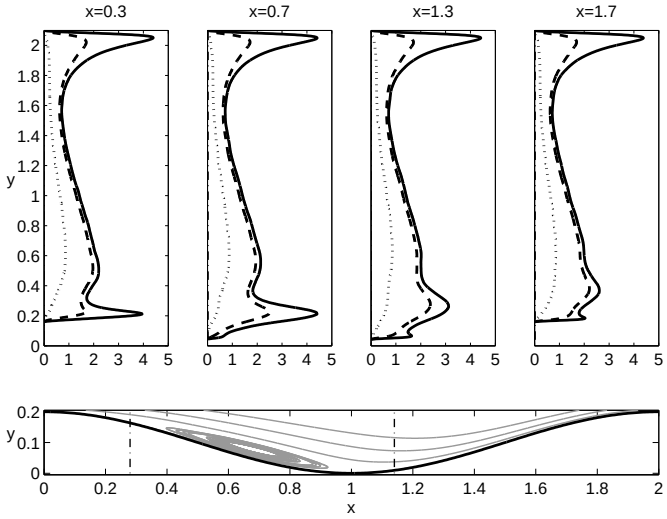

Figure 6.13: Profiles of $\overline{u'\theta'_s}$. Solid lines are for Pr=0.71, dashed lines are for Pr=0.20, dotted lines are for Pr=0.025. At the bottom, dash-dot lines indicate the separation and reattachment locations.

Profiles of the streamwise and vertical components of the turbulent heat fluxes are drawn respectively in figure 6.13 and figure 6.14. The results obtained for Pr=0.025 are consistent with the laminar profiles of the correspondent averaged thermal field. Figures 6.13 and figure 6.14 show that the results obtained for Pr=0.20 and Pr=0.71 markedly diverge in the

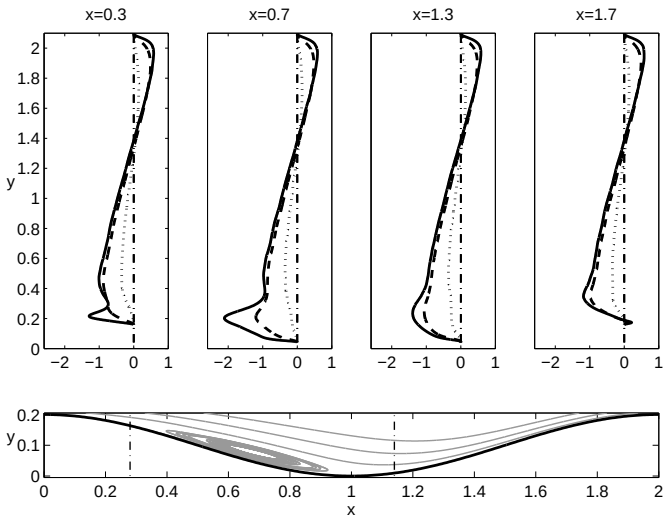

Figure 6.14: Profiles of $-\overline{v'\theta'_s}$. Solid lines are for Pr=0.71, dashed lines are for Pr=0.20, dotted lines are for Pr=0.025. At the bottom, dash-dot lines indicate the separation and reattachment locations.

near wall regions, as much as the separated flow region is approached, while they almost overlap in the channel core. Larger peaks are obtained for Pr=0.71. The profiles of $\overline{u'\theta'_s}$, figure 6.13, show a peak at a distance from the wall which corresponds to the separated shear layer. Moving from the separated flow regions on the down slope portion of the wave, *i.e.* $x = 0.3$ and $x = 0.7$, to the attached flow regions on the up-slope portion of the wave, *i.e.* $x = 1.3$ and $x = 1.7$, the peak of $\overline{u'\theta'_s}$ occurring in correspondence of the shear layer becomes less intense, and a further peak appears within the thermal boundary layer, which is locally very thin. The profiles of the vertical component of the turbulent heat fluxes $\overline{v'\theta'_s}$, figure 6.14, also peak in correspondence to the separated

shear layer. In the fully accelerated boundary layer which develops on the up-slope portion of the wavy wall, *i.e.* $x = 1.7$, the profile of $\overline{v'\theta'_s}$ changes sign and becomes negative, very similarly to the local behavior of the Reynolds stress profile. Also, the turbulent contribution to the vertical heat fluxes has locally the same sign of the advective contribution $-\overline{v}\overline{\theta_s}$, in fact both $\overline{\theta_s}$ and $\overline{v}$ are positive in this region, and it is noticed that such a concordance occurs even where a peak Nusselt number is found, as can be seen from figure 6.17.

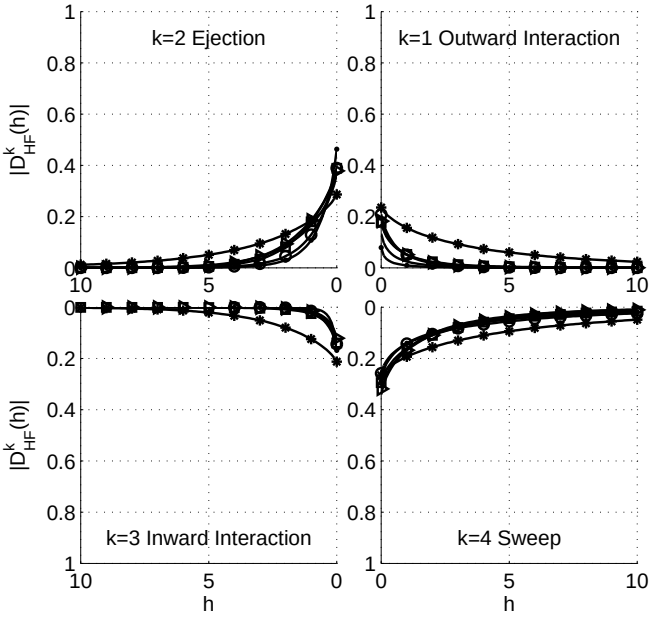

Figure 6.15: Quadrant-hole analysis of turbulent heat fluxes for subsequent axial positions at $y^+ = 10$. Circles correspond to $x = 0.1$, dots to $x = 0.3$ squares to $x = 0.5$, triangles to $x = 1.0$ and asterisks to $x = 1.5$. Solid blue lines indicate reference data.

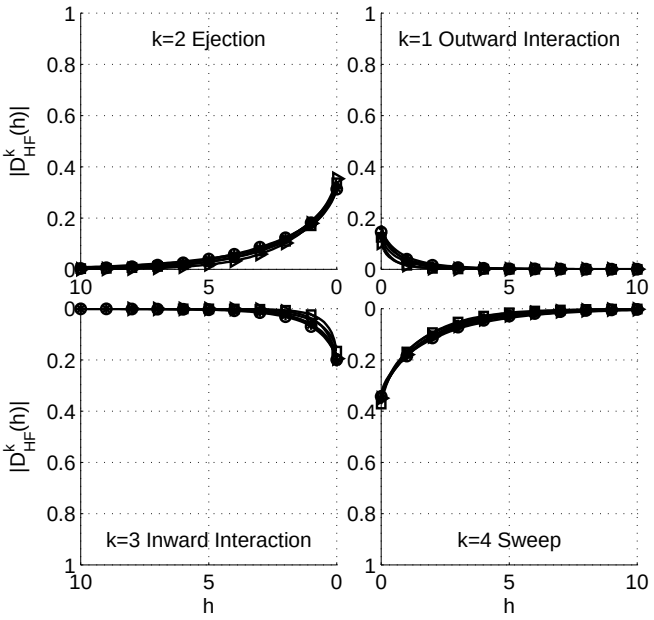

Figure 6.16: Quadrant-hole analysis of Reynolds stress for subsequent axial positions at $y^+ = 50$. Circles correspond to $x = 0.1$, dots to $x = 0.3$ squares to $x = 0.5$, triangles to $x = 1.0$ and asterisks to $x = 1.5$. Solid blew lines indicate reference data.

As for the Reynolds stress, a quadrant-hole analysis is conducted to investigate on the events contributing to the production of turbulent heat fluxes. The quadrant contributions to the total averaged value of turbulent heat flux $D^k_{HF}(h)$ are calculated similarly as for Reynolds stress, section 6.1. Quadrant-hole analysis has been performed for the same subsequent axial positions and two different vertical distances from the wall $y^+ = 10$ and $y^+ = 50$, as considered for the quadrant-hole analysis of Reynolds stress. Further, the re-

sults obtained at the flat wall do not depend significantly on x and the contribution $\phi^k_{HF}(h)$ calculated on the upper flat wall is referred to as *reference data* in the following discussion. Figure 6.15 shows that sweep is the leading mechanism in the formation of turbulent heat fluxes for all $y^+ = 10$ locations. For $x = 1.5$, outward interactions contribute in a large part as well, but they prevail only at smaller distances from the wall, where also the turbulent heat flux in y direction becomes negative. At a larger distance from the wall, for $y^+ = 50$, the quadrant analysis results are very close to the reference data, figure 6.15, more close for turbulent heat flux than for the Reynolds stress.

Nusselt number

	Pr = 0.025	Pr = 0.20	Pr = 0.71
Nu	12.2	37.1	77.3

Table 6.2: Global values of the Nusselt number.

Profiles of the local Nusselt number Nu(x), equation (3.34), are represented in figure 6.17. The profile of Nu(x) at the upper flat wall is almost perfectly horizontal, thus indicating that the undulation of the lower wall does not influence significantly the heat transfer rate at the upper wall of the channel. As the Prandtl number decreases from 0.71 to 0.025 both the local and global Nusselt number decreases too, see also table 6.2, and this can be ascribed to the laminarization of the heat transport as the molecular Prandtl number decreases from 0.71 to 0.025. The Nu(x) profile at the wavy wall shows a local minimum after the separation point, and

a local maximum at the up-slope portion of the wave. The locations of Nusselt minima and maxima move downstream for decreasing Prandtl number value. The relative difference between the maximum and minimum Nusselt value, ΔNu, with respect to the mean value of the Nusselt number at the flat wall, $\Delta Nu/Nu_{w,u}$ decreases for decreasing the Prandtl number, from 1.39 for Pr = 0.71, to 1.27 for Pr = 0.20 and 1.05 for Pr = 0.025, thus showing that the flow separation and reattachment affect the heat transfer rate as much as the Prandtl number of the fluid increases from 0.025 to the almost unity value 0.71.

Turbulent Prandtl number

The turbulent Prandtl number is an important parameter for practical heat transfer analyses.

$$\mathrm{Pr}_t = \frac{\overline{u'v'}\,\dfrac{\partial\overline{\theta_s}}{\partial y}}{\overline{v'\theta'_s}\,\dfrac{\partial\overline{u}}{\partial y}} \tag{6.8}$$

The turbulent Prandtl number is widely used in the turbulence diffusion models, and often it is assumed to be constant and unity, at least for molecular Prandtl number equal or greater than one. A number of correlations have been also proposed, which take into account of the Pr_t dependence on the molecular Prandtl number and the wall-normal distance (Kays 1994).

The evaluation of the turbulent Prandtl number is of great interest for the present case study, where also not unity molecular Prandtl number are investigated and a very different flow

dynamics develops in the region of the upper-flat wall and lower-wavy wall.

The equation (6.8) has been evaluated on the base of DNS results. The wall-normal profiles of turbulent Prandtl number in the region close to the upper flat wall are represented in figure 6.18. For Pr = 0.71 the Pr_t is almost uniform and around unity, and for Pr = 0.20 it only slightly diverges from this trend. Instead, for Pr = 0.025 the profile shape is rather different and higher values are obtained, given a less intensity of the term $\overline{v'\theta'_s}$ in this case.

When turbulent convection is calculated over a non-planar surface and the flow separates, not only the Pr_t diverges from unity but it also loses its significance locally. Maps of the turbulent Prandtl number in the lower portion of the channel are represented in figure 6.19. The range of values around unity, $0.6 < \mathrm{Pr}_t < 1.4$, has been selected to discriminate the regions of the domain where Pr_t largely diverges form unity, and going also to $\pm\infty$, from the regions where it stays around unity. For the Pr = 0.71 case, figure 6.19(a), the turbulent Prandtl number value diverges very close to the wall and in the areas localized up to the crest of the wave. A very similar Pr_t map is obtained for the Pr = 0.20 case. For the Pr = 0.025 case, as figure 6.19(b) shows, the equation (6.8) provides diverging values for larger areas and more irregularly distributed with respect to the $\mathrm{Pr} \sim 1$ case.

Critical analysis of different turbulent diffusion models

A common practice in the turbulence modeling is to employ the standard gradient diffusion hypothesis (SGDH) for repro-

duce the turbulent thermal fluxes. The SGDH model provides for the present turbulent thermal flux components this formulation:

$$\overline{u'\theta'_s} = -\frac{\nu_t}{\mathrm{Pr}_t}\frac{\partial\overline{\theta_s}}{\partial x} \tag{6.9}$$

$$\overline{v'\theta'_s} = -\frac{\nu_t}{\mathrm{Pr}_t}\frac{\partial\overline{\theta_s}}{\partial y} \tag{6.10}$$

As highlighted in chapter 2 this approach provides a rather rough approximation of the turbulent heat fluxes, also for the basic case of the turbulent flat channel.

In the following, three different turbulence diffusion models are encompassed. Their accuracy into predict the scalar flux components, $\overline{u'\theta'}$ and $\overline{v'\theta'}$, is assessed against the DNS results. The variables used in the models formulation are those calculated with the present DNS, in order to discriminate the only errors due to the scalar transport modeling.

The selected turbulence diffusion models are those based on the standard gradient diffusion hypothesis (SGDH), the general gradient diffusion hypothesis (GGDH) by Daly and Harlow (1970) and the high order-general gradient diffusion hypothesis (HO-GGDH) by Abe and Suga (2001). The GGDH model assumes for the present case the form:

$$\overline{u'\theta'_s} = C_\theta\tau_c\left(\overline{u'^2}\frac{\partial\overline{\theta_s}}{\partial x} + \overline{u'v'}\frac{\partial\overline{\theta_s}}{\partial y}\right) \tag{6.11}$$

$$\overline{v'\theta'_s} = C_\theta\tau_c\left(\overline{u'v'}\frac{\partial\overline{\theta_s}}{\partial x} + \overline{v'^2}\frac{\partial\overline{\theta_s}}{\partial y}\right) \tag{6.12}$$

where C_θ is a model constant, and τ_c the characteristic time-scale, correspondent to the ratio between the turbulent

kinetic energy and its dissipation rate (k/ϵ). The GGDH can be considered an improved version of the SGDH, as it also takes into account the non-alignment of the turbulent scalar fluxes and the mean temperature gradient.

The HO-GGDH model is an high-order extension of the GGDH:

$$\overline{u'\theta'_s} = C_\theta \frac{\tau_c}{k} \left(\overline{u'^2}^2 \frac{\partial \overline{\theta_s}}{\partial x} + \overline{u'v'}^2 \frac{\partial \overline{\theta_s}}{\partial x} + \overline{u'^2}\,\overline{u'v'} \frac{\partial \overline{\theta_s}}{\partial y} + \overline{v'^2}\,\overline{u'v'} \frac{\partial \overline{\theta_s}}{\partial y} \right) \tag{6.13}$$

$$\overline{v'\theta'_s} = C_\theta \frac{\tau_c}{k} \left(\overline{u'^2}\,\overline{u'v'} \frac{\partial \overline{\theta_s}}{\partial x} + \overline{v'^2}\,\overline{u'v'} \frac{\partial \overline{\theta_s}}{\partial x} + \overline{u'v'}^2 \frac{\partial \overline{\theta_s}}{\partial y} + \overline{u'^2}^2 \frac{\partial \overline{\theta_s}}{\partial y} \right) \tag{6.14}$$

A preliminary discussion is performed for the flat channel flow, before to investigate the more complex case of the separated wavy channel flow. The DNS data by Kawamura et al. (1998) have been used in this case for the models variables and as reference data for the models predictions of $\overline{u'\theta'_s}$ and $\overline{v'\theta'_s}$. The values of the scalar fluxes provided by the DNS and by the diffusion models are of different order of magnitude: the SGDH and GGDH predictions are greater than the DNS results of $O(10^1)$, the HO-GGDH predictions are greater than the DNS results of $O(10^3)$. For this reason the assessment of the selected scalar fluxes models is performed just by comparing the unit vector parallel to $\overline{\mathbf{u}'\theta'_\mathbf{s}}$ as predicted by the DNS and by the thermal diffusion models. The unit vectors parallel to $-\overline{\mathbf{u}'\theta'_\mathbf{s}}$, as predicted by the present DNS and by the three diffusion models selected, are depicted in figure 6.20. Four different distances from the wall are considered. The results obtained for Pr = 0.20 are not shown here as they are very

similar to those obtained for Pr = 0.71, consistently with the similar distribution of the correspondent turbulent Prandtl number and of the mean temperature gradients. From both the figures 6.20(a) and 6.20(b) it can be seen that the GGDH model approximates the DNS results at best, but its performance gets worse as moving far from the wall. The predictions of the HO-GGDH model are instead closer to the DNS results for larger distances from the wall. From the comparison of the results obtained for Pr = 0.025 and Pr = 0.71 it seems that the modeled fluxes do to not change with the Prandtl number, as opposed to the DNS predictions.

The results obtained in the case of the wavy channel are represented in figure 6.21 for the different streamwise locations $x = 0.3, 0.7, 1.3, 1.7$. The results for Pr = 0.20 are quite similar to those obtained for Pr = 0.71, and they are not represented. In this case the accuracy of the selected turbulence models varies significantly with both the vertical and the streamwise coordinate. The GGDH model predictions are in general in a better agreement with the present DNS results. The results of the GGDH and HO-GGDH models are in a fairly good agreement in the mean recirculation region, where their accuracy seems to be not compromised by the separated flow conditions. The SGDH, instead, behaves locally at worst, even by predicting wrong the sign of the streamwise component of the scalar fluxes. By comparing the figures 6.21(a) and (b) the models predictions appear as not significantly affected by the Prandtl number variation, as observed in the flat channel case, and this confirms the validity of the assumption of a constant turbulent Prandtl number in eddy-diffusivity models.

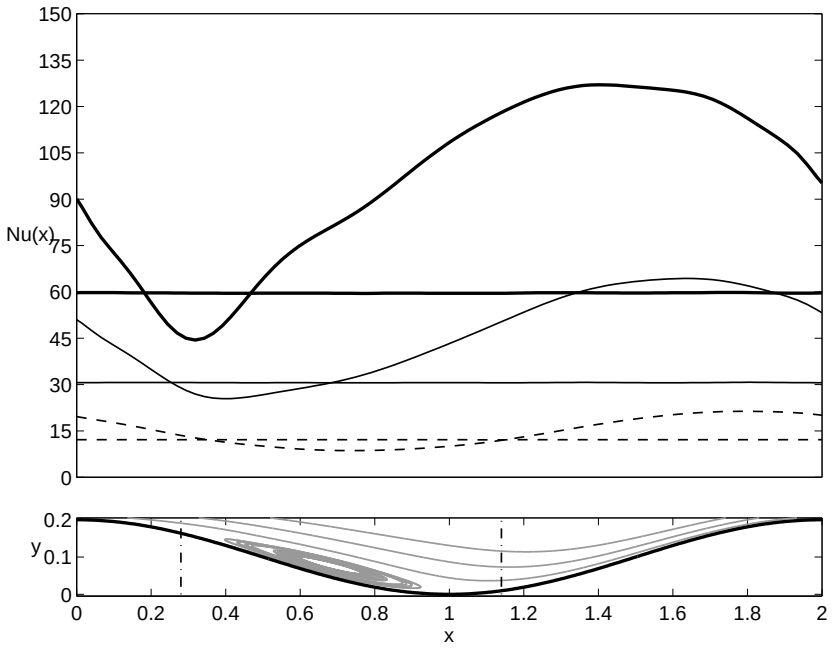

Figure 6.17: Profiles of the local Nusselt number: the straight lines represent $\mathrm{Nu}(x)$ at the upper wall, the curved lines represent $\mathrm{Nu}(x)$ at the lower wall. Thick-solid lines are for Pr=0.71, thin-solid lines are for Pr=0.20, thin-dashed lines are for Pr=0.025. At the bottom, dash-dot lines indicate the separation and reattachment locations.

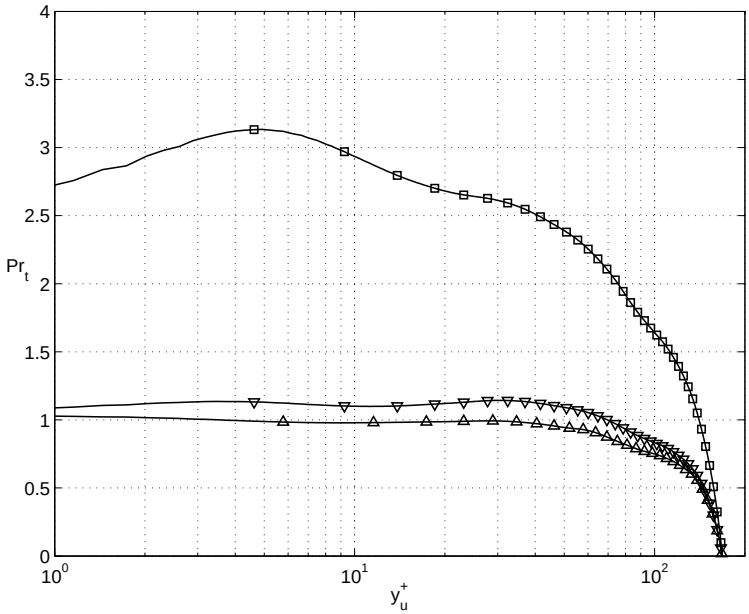

Figure 6.18: Vertical profile of turbulent Prandtl number averaged on x in the region close to the flat wall. Upward-pointing triangles correspond to Pr = 0.71, downward-pointing triangles to Pr = 0.20, squares to Pr = 0.025.

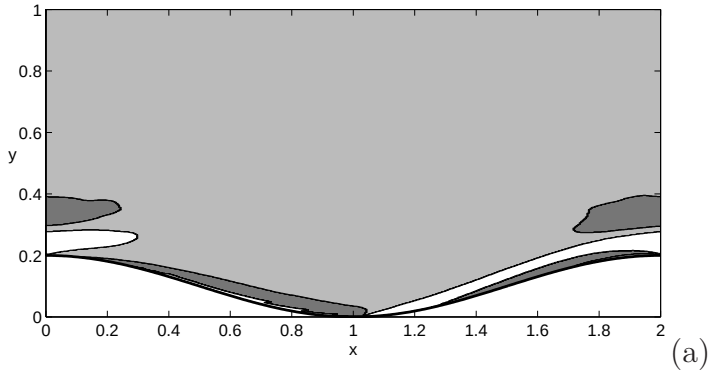

(a)

(a) Pr = 0.71

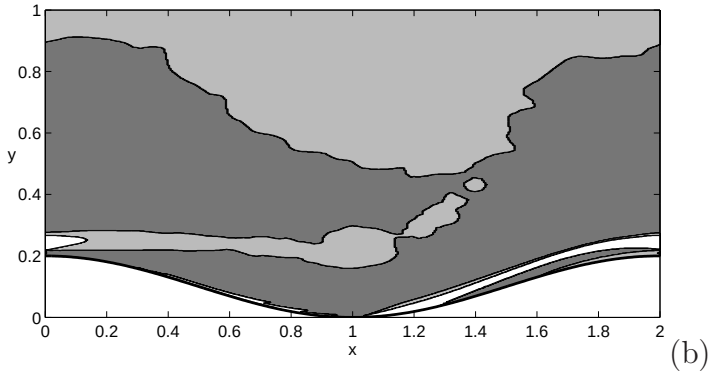

(b)

(b) Pr = 0.025

Figure 6.19: Map of the turbulent Prandtl number in the lower portion of the channel. Dark-grey is for $\mathrm{Pr}_t > 1.4$; light-grey for $0.6 < \mathrm{Pr}_t < 1.4$ and white for $\mathrm{Pr}_t < 0.6$.

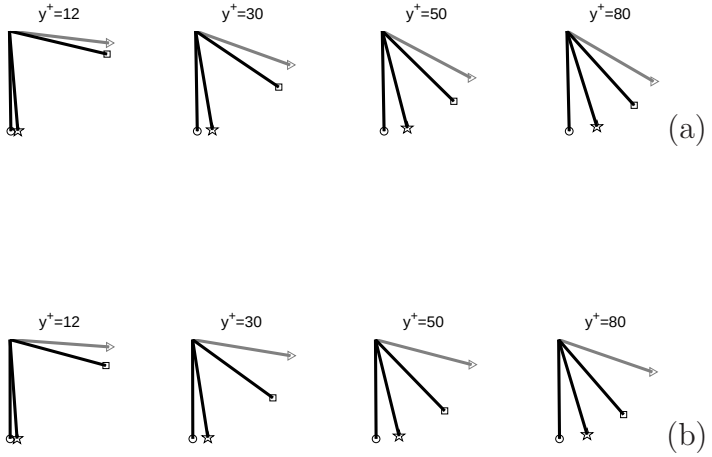

Figure 6.20: Unit vectors of the averaged turbulent heat fluxes $\overline{\mathbf{u}'\theta'_{\mathbf{s}}}$ for the flat channel case. (a) Pr = 0.71; (b)Pr = 0.025. Gray arrows are for DNS results, square arrows head forthe GGDH model, star arrows head for the HO-GGDH and circle arrows head for the SGDH model.

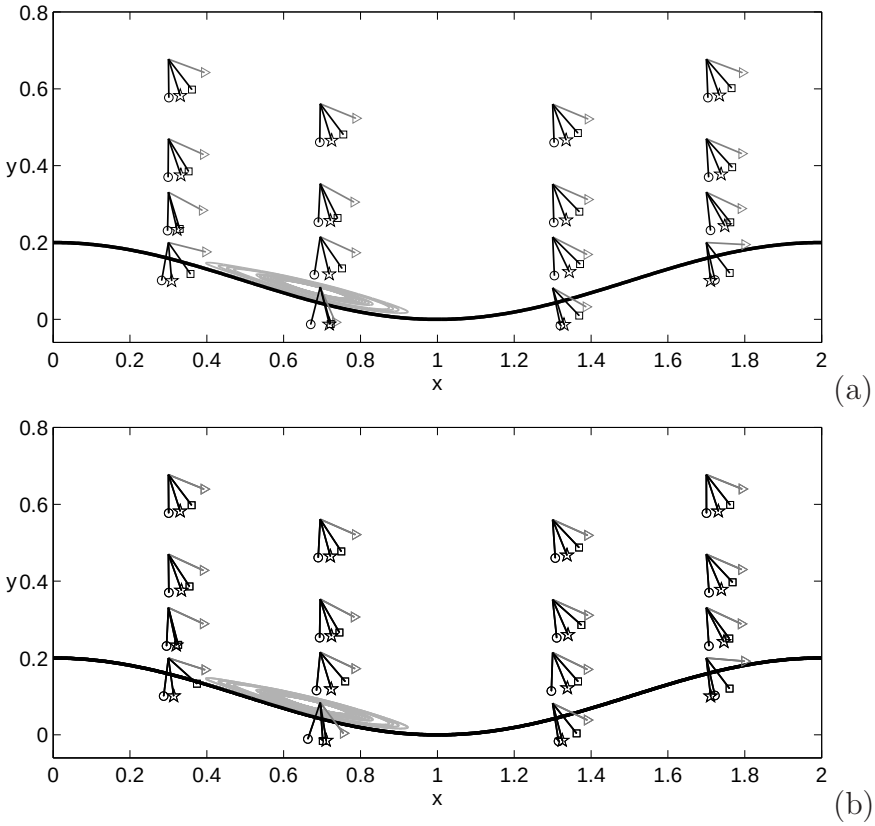

Figure 6.21: Unit vectors of the averaged turbulent heat fluxes $\overline{\mathbf{u}'\theta'_{\mathbf{s}}}$. (a) Pr = 0.71; (b)Pr = 0.025. Gray arrows are for DNS results, square arrows head for the GGDH model, star arrows head for the HO-GGDH and circle arrows head for the SGDH model.

Chapter 7

Results of RANS simulations

In this chapter the results obtained by RANS simulations for $\mathrm{Re} = 19\,000$ and only one Prandtl number value $\mathrm{Pr} = 0.71$ are presented. The two-equations eddy-viscosity models k-ω SST (Menter 1993) and q-ζ model (Gibson and Dafa'Alla 1995) are used for the modeling of the Reynolds stress, and the standard gradient-transport model is used for reproduce the turbulent heat fluxes.
The results provided by DNS, averaged over the time and the spanwise direction z, are also reported for comparative purposes. Both results by RANS and DNS simulations are shown averaged over one periodicity of the channel, and they are presented in terms of the non-dimensional variables.

7.1 Velocity field

Figure 7.1 shows the streamlines and velocity magnitude contours of the averaged velocity field as obtained by the two

	DNS		q-ζ model		k-ω SST	
	x_s	x_r	x_s	x_r	x_s	x_r
$\mathrm{Re} = 19\,000$	$0.14\,\lambda$	$0.55\,\lambda$	$0.14\,\lambda$	$0.47\,\lambda$	$0.12\,\lambda$	$0.70\,\lambda$

Table 7.1: Flow separation and reattachment locations.

encompassed eddy-viscosity models and by DNS for the selected Reynolds number $\mathrm{Re} = 19\,000$. Both the RANS models successfully predict the occurrence of separated flow conditions, with a fair agreement with DNS. Locations where flow separation (x_s) and reattachment (x_r) are detected by the different numerical methods are listed in table 7.1. The separation point is captured properly by both models, while the q-ζ model is found to be more accurate in predicting the reattachment point. Both RANS models show much thicker recirculating regions as compared to the DNS results. In particular, the mean vortex predicted by the k-ω SST model is remarkably bigger.

It is interesting to note that k-ω SST velocity contours are almost flat, as if little affected by the wall shape. This is due to the fact that, in this case, the separated flow almost covers the entire area between the crests of the wavy wall. Due to the different sizes and shapes of the mean vortices, contours are more distorted for q-ζ and DNS instead, the main flow being deviated towards the ascending segment of the wall.

Above the recirculating region a separated turbulent shear layer develops, thus raising the turbulence intensity. The velocity maps of figure 7.1 suggest that DNS and RANS computations provide different extension of such region, where strong vertical velocity gradients occur. In particular, it can

be inferred that the shear layer modeled by RANS is considerably thinner, and placed at a smaller distance from the wavy wall. This is confirmed also by the qualitative profiles of turbulent kinetic energy reported in figure 7.2. Peaks of k predicted by DNS are found further from the wall than those predicted by RANS models; the same holds for the location where the free-stream value is approached. It is interesting to note that such peaks are not even always present in RANS profiles, hence corroborating the above observations.

Figures from 7.3 to 7.5 report the profiles of the second order moment $-\overline{u'v'}$, as extracted from the DNS data and reconstructed from RANS results. All profiles are scaled by their maximum value. A qualitative analysis indicates that the q-ζ model gives results which are comparable to those obtained by DNS, especially in the vicinity of the upper flat wall. Once again, in the turbulent shear layer, the DNS predict sharp peaks of the Reynolds stresses that are underestimated by RANS models. Sign inversions of the second order moment past the reattachment point are also detected by direct simulations. Once again, such features cannot be found in the RANS profiles: this confirms the fact that RANS models predict stronger velocity gradients in the vicinity of the wavy wall, when compared to DNS. As already observed for k, the intensity of the fluctuations in the core flow predicted by RANS models is comparable with the peak values close to the lower wall. This is especially true for the k-ω SST.

A further parallelism between DNS and RANS results can be observed in the profiles of $-\overline{u'v'}$. The second order moment changes its sign halfway through the vertical extension of the channel. The vertical location of such a sign inversion predicted by DNS is fairly well reproduced by both RANS

models. This confirms the overall adequacy of both q-ζ and k-ω SST turbulence models for the simulation of the effect of separation on the main flow.

7.2 Temperature field

Maps of the averaged temperature field in the vicinity of the wavy wall are depicted in figure 7.6. In the case of RANS, turbulent transport of thermal energy is modeled by employing a fixed turbulent Prandtl number, equal to $\mathrm{Pr}_t = 0.85$. The features of the RANS-obtained thermal fields largely depend on the computed flow field and, consequently, on the turbulence model adopted.

The comparison of RANS results with DNS brings forth some remarkable concordances and discrepancies. Firstly, a look at the temperature contours of figure 7.6 suggests that peaks of the heat transfer rate are present in the separation and reattachment areas, whilst the thermal boundary layer enlarges within the boundaries of the recirculation regions, creating lower temperature gradients. Such features are observable both on DNS and RANS results. It is to be noted that the position and size of the low-temperature spots are coherent with the predicted size of the recirculation zones; hence, these appear as more pronounced in the temperature maps related to RANS results (figure 7.6(b) and (c)). On the other hand, the thermal boundary layer past the reattachment point appears slightly thinner in RANS results, if compared to DNS. Such a tendency can be ascribed to the overprediction of near-wall velocity gradients already observed for RANS models, and it is confirmed by the qualitative profiles of figures 7.7, 7.8 and 7.9, where fluctuations of the vertical con-

vective fluxes are plotted at selected streamwise locations. As a matter of fact, the RANS-obtained profiles exhibit strong negative peaks of the turbulent fluctuations near the wavy wall, as a result of higher vertical temperature gradients.

DNS	q-ζ	k-ω
76.2	117.6	60.5

Table 7.2: Global Nusselt number values.

Nusselt number

Table 7.2 reports the global Nusselt number values obtained by the different numerical methods encompassed. It is seen that the q-ζ model, although providing a good qualitative representation of the mean flow and temperature field, overestimates the Nusselt number by a rough 50% with respect to the DNS data, whilst the k-ω SST provides a closer, slightly underestimated guess, in spite of its worse overall agreement with DNS results. Such apparent discrepancies are instead explainable by the observations brought forth in the previous discussion. All the results suggest that, globally, the effect of turbulence on flow and heat transfer is significantly overpredicted by RANS models with respect to the directly simulated regimes. In turn, higher wall temperature gradients are computed past the reattachment point, thus justifying the results obtained by the q-ζ model. As for the $k-\omega$ SST result, it can be explained by the prediction of a larger recirculation zone, which, as already observed, is associated with a wider region of low heat transfer rates, thus compensating the high gradients in the ascending section of the wavy wall.

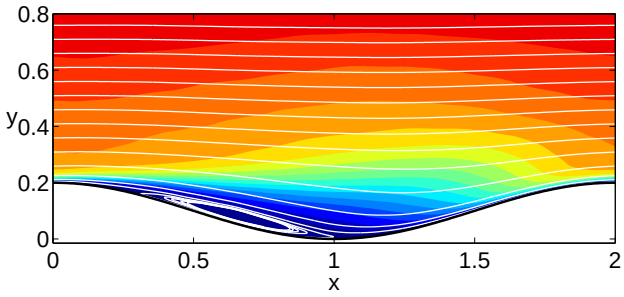

(a) DNS

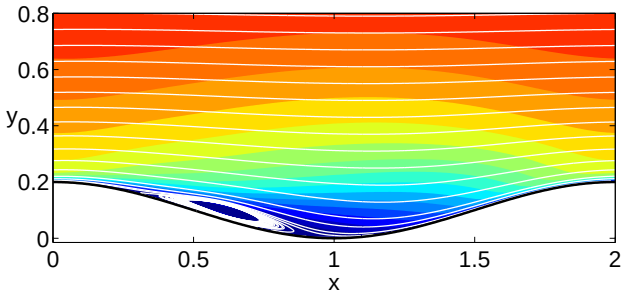

(b) q-ζ model

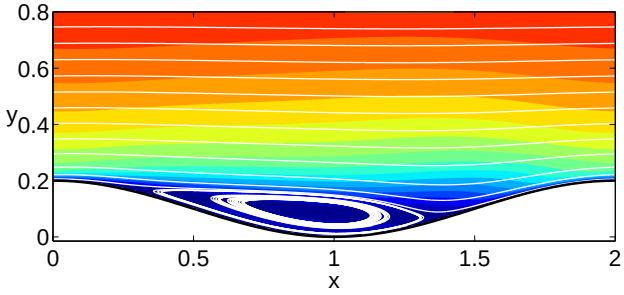

(c) k-ω SST model

Figure 7.1: Streamlines and contours of the time-averaged velocity module for $\mathrm{Re} = 19\,000$. Mean flow direction is from left to right.

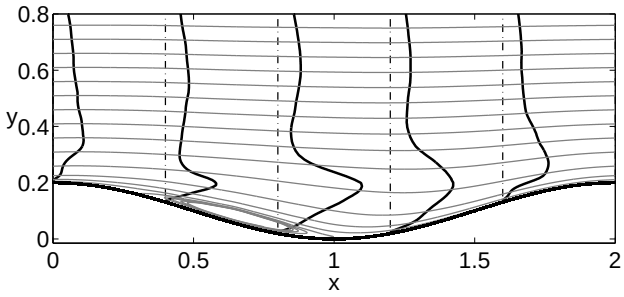

(a) DNS

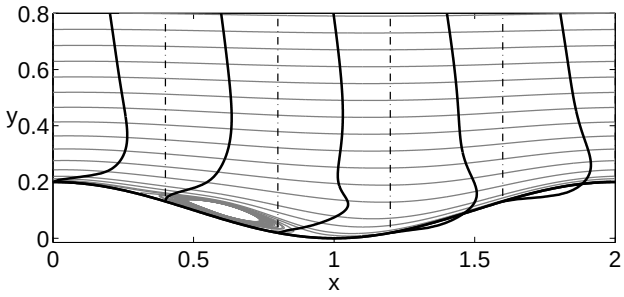

(b) q-ζ model

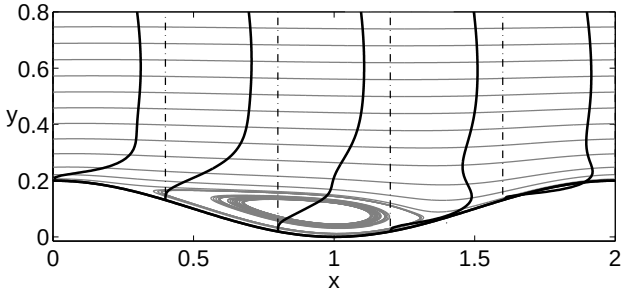

(c) k-ω SST model

Figure 7.2: Profiles of turbulent kinetic energy together with streamlines for Re = 19 000. Mean flow direction is from left to right. All profiles are scaled by their maximum value.

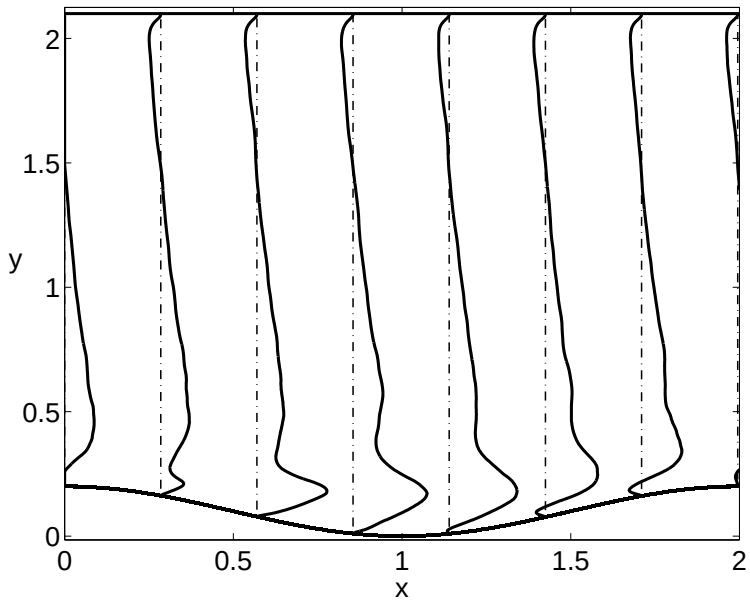

Figure 7.3: Profiles of $-\overline{u'v'}$ obtained by DNS for Re = 19 000.

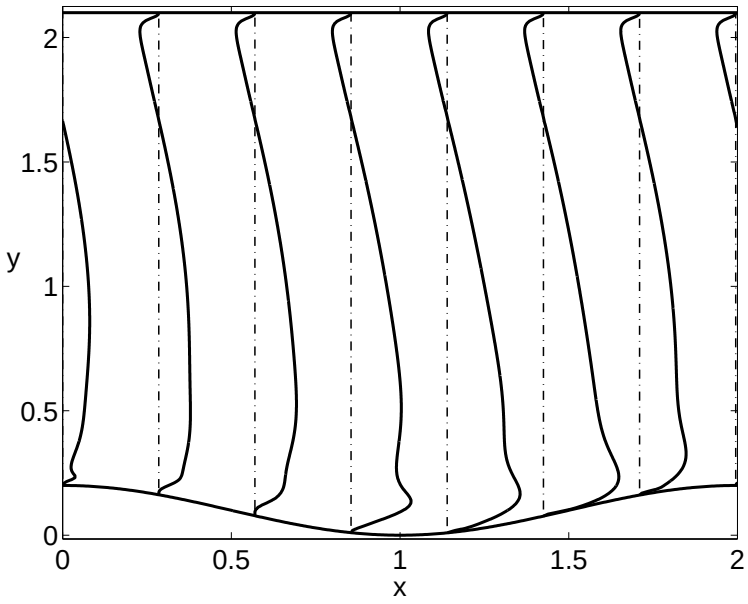

Figure 7.4: Profiles of $-\overline{u'v'}$ reconstructed by q-ζ model data for $\mathrm{Re} = 19\,000$.

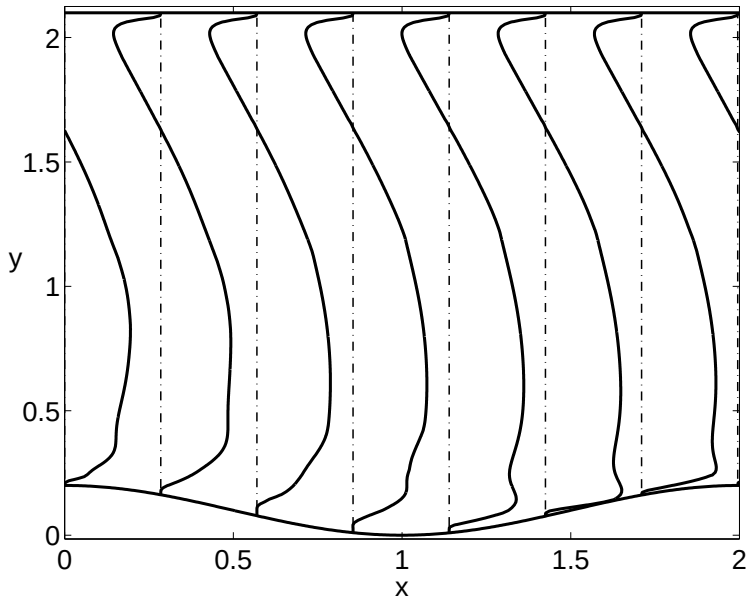

Figure 7.5: Profiles of $-\overline{u'v'}$ reconstructed by k-ω SST model data for $\mathrm{Re} = 19\,000$.

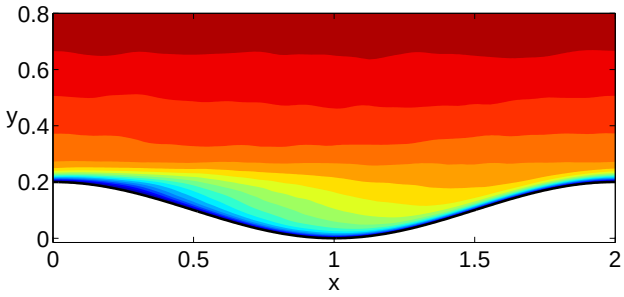

(a) DNS

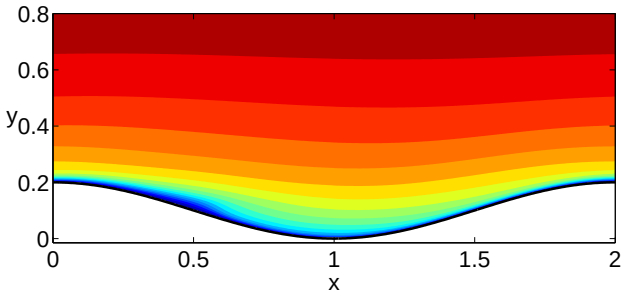

(b) q-ζ model

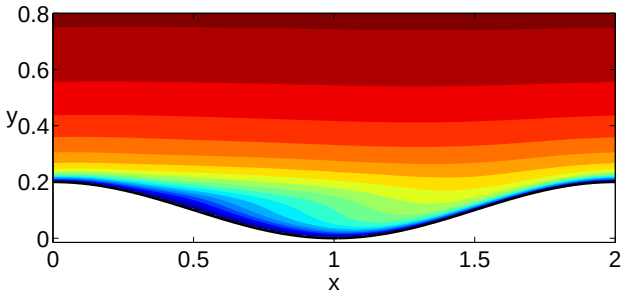

(c) k-ω SST model

Figure 7.6: Contours of the time-averaged periodic thermal field for $\mathrm{Re} = 19\,000$ and $\mathrm{Pr} = 0.71$.

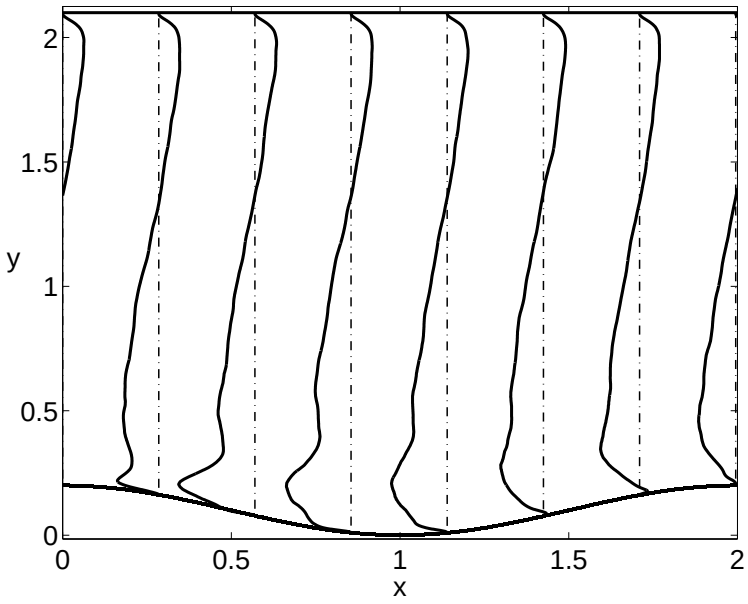

Figure 7.7: Profiles of $\overline{v'T'}$ obtained by DNS for $\mathrm{Re} = 19\,000$ and $\mathrm{Pr} = 0.71$.

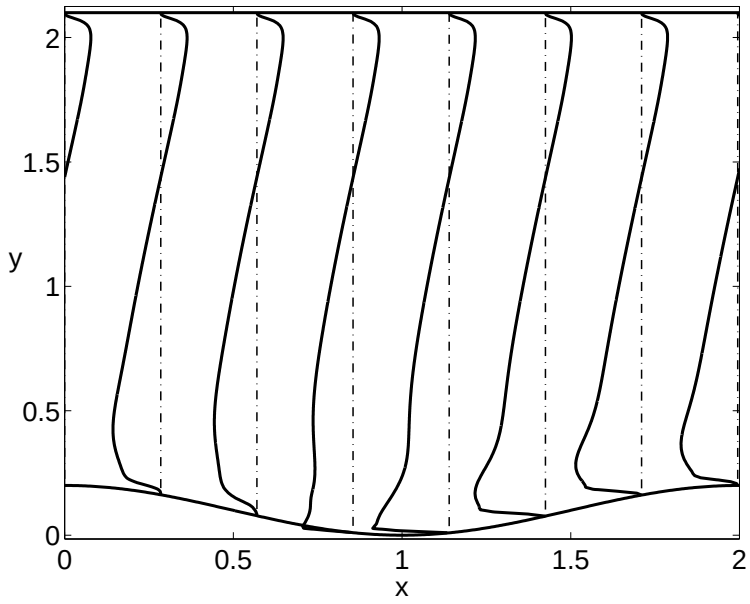

Figure 7.8: Profiles of $\overline{v'T'}$ reconstructed by q-ζ model data for $\mathrm{Re} = 19\,000$ and $\mathrm{Pr} = 0.71$.

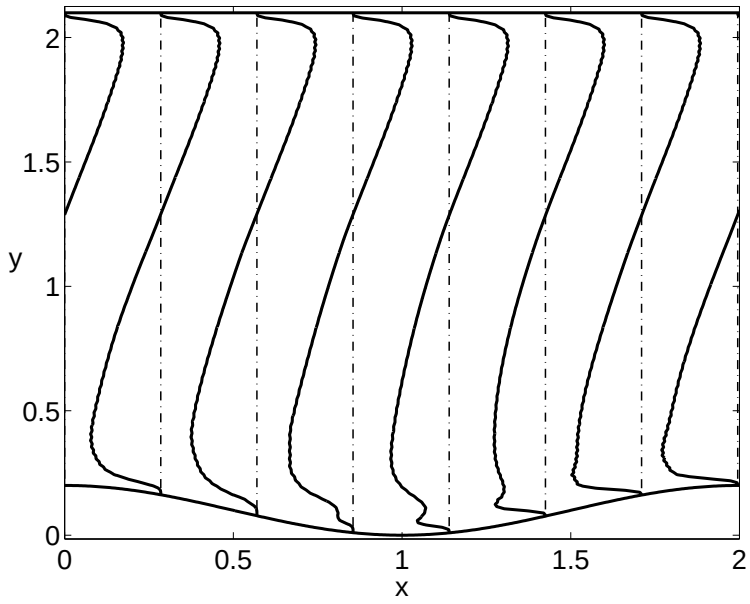

Figure 7.9: Profiles of $\overline{v'T'}$ reconstructed by k-ω SST model data for $\mathrm{Re} = 19\,000$ and $\mathrm{Pr} = 0.71$.

Chapter 8

Conclusions

In this work the problem of turbulent forced convection in a channel with one wavy wall and one flat wall has been numerically investigated. The numerical simulations have been conducted for a Reynolds number $\mathrm{Re} = 19\,000$, based on the mean bulk velocity and hydraulic diameter. The flow has been assumed incompressible, fully developed and driven by a constant pressure drop. The channel walls have been considered at a uniform temperature. Three different values of the Prandtl number have been investigated: $\mathrm{Pr} = 0.025$, which corresponds to the liquid Lead-Bismuth Eutectic, $\mathrm{Pr} = 0.2$, which corresponds to Helium-Xenon gas mixture, and $\mathrm{Pr} = 0.71$, which corresponds to air. The buoyancy effects have been neglected, the temperature is a passive scalar, and three different temperature fields have been calculated for the three different Prandtl number values.

By means of direct numerical simulations both the effects of the wavy wall shape and the Prandtl number on the heat transport mechanisms have been analyzed. Also with use of DNS results, the reliability of some largely used

eddy-diffusivity models has been evaluated in relation to the separated flow conditions and the non-unity Prandtl number values. Further, by means of RANS simulation, the performance of two different eddy-viscosity turbulence models, the k-ω SST model (Menter 1993) and q-ζ model (Gibson and Dafa'Alla 1995), selected for their good characteristics, is assessed against the DNS results.

A validation study has been conducted for the DNS method. For the validation of the DNS method a direct simulation for a Reynolds number of Re = 13 700 based on the mean velocity and the hydraulic diameter has been performed, which is comparable with those of reference data, the experiments by Hudson (1993) and DNS data by Cherukat et al. (1998), available for the velocity field. The profiles of the main averaged quantities and first order moments provided by the present DNS have been successfully compared with both the experiments and previous DNS data.

For the discussion of the DNS results, the mean quantities have been averaged over the three waves and the spanwise length L_z, besides being integrated in time. For the selected flow regime, the mean flow separates past the crest and reattaches past the thought of the wave. A separated shear layer is observed above the mean recirculation region. In the separated shear layer and in correspondence of the restart of boundary layer, at the flow reattachment position, the velocity fluctuations are very intense, and this confirms the beneficial effects of flow separation and reattachment on the turbulent mixing. A change of sign in the Reynolds stress profiles is observed on the up-slope portion of the wave, where also the outward interactions represent the main contribution to the Reynolds stress. Due to the separated flow region, the

friction factor on the wavy wall is smaller than on the upper flat wall. The friction factor on the upper wall is instead larger than the value given for a flat channel case at the same Reynolds number, as in this case the undulation of the lower wall increases the flat wall drag.

The temperature field results to depend strongly on the Prandtl number investigated. The mean temperature profiles display a typical turbulent shape in the $\mathrm{Pr} = 0.71$ case, while a laminar profile corresponds to $\mathrm{Pr} = 0.025$, although the velocity field is the same. The temperature distribution calculated for $\mathrm{Pr} = 0.20$ follows more closely results for $\mathrm{Pr} = 0.71$. Also, the maps of the instantaneous temperature fields show that a greater difference between the largest eddies and the smallest one occur as the Prandtl number increases from 0.025 to 0.71. On the up-slope portion of the wavy wall, the profiles of the vertical turbulent heat flux change sign, very similarly to the local behavior of the Reynolds stress. A peak heat transfer rate is calculated locally, while a minimum heat transfer rate corresponds to the region after the separation point. As the Prandtl number decreases from 0.025 to 0.71 the effects of flow separation and reattachment on the heat transfer rate are less intense, and the Nusselt number decreases both locally and globally. The undulation of the lower wall does not influence significantly the heat transfer rate at the upper flat wall, where an almost flat profile of the Nusselt number is obtained. Over the non-planar surface, where the flow separates, the Pr_t loses its significance locally: diverging values are calculated, and for larger areas as much as the molecular Prandtl number diverges from unity.

From the assessment of the turbulence diffusion models, standard gradient diffusion hypothesis (SGDH), general gradi-

ent diffusion hypothesis (GGDH) and high order-general gradient diffusion hypothesis (HO-GGDH), it results that their accuracy into predict the turbulent heat fluxes varies significantly with both the vertical and the streamwise coordinate. The GGDH model predictions are in general in a better agreement with the present DNS results. The SGDH model, which is the most commonly used for the modeling of turbulent thermal fluxes, in the separated flow region does not even able to predict the sign of the streamwise component of the scalar fluxes. The models predictions seem to be not significantly affected by the Prandtl number variation, and this confirms the validity of the assumption of a constant turbulent Prandtl number in eddy-diffusivity models.

Results by RANS simulations, for $\mathrm{Re} = 19\,000$ and only one Prandtl number value, $\mathrm{Pr} = 0.71$, indicate that both the selected eddy-viscosity turbulence models, the k-ω SST and q-ζ models, are able to predict the occurrence of flow separation. Both RANS models predict successfully the separation location, while a thicker recirculation region and a different reattachment location result with respect to the DNS data. Also, the shear layer modeled by RANS is considerably thinner and closer to the wavy wall.

The position and size of the low-temperature spots are coherent with the predicted size and extent of the recirculation zones, hence, these appear as more pronounced in the temperature maps related to RANS results. All the results suggest that, globally, the effect of turbulence on flow and heat transfer is significantly overpredicted by RANS models with respect to the directly simulated regimes. In general, the q-ζ model demonstrates itself to be in a better agreement with the DNS predictions of mean flow and temperature pat-

terns. Instead, a less satisfactory concordance is found on the average heat transfer rates: the q-ζ model overestimates the Nusselt number by a rough 50% with respect to the DNS data.

Even if the flow separation is often used for heat transfer enhancement, the mechanisms which are responsible of the heat transfer increase are not fully understood yet, and turbulence models commonly used are often not adequate for investigating such phenomena. This is currently an open issue which should be fully recognized by the scientific and applied research community.

Part of the work performed in this thesis focused on heat transfer in liquid metals. Given the high density of these fluids, practical Reynolds number are rather high. It is clear from results given in the selected flow regime that the use of liquid metals in cooling systems would be advantageous for example in terms of safety, but not for enhancing the heat transport with respect to the fluids with Prandtl number of order unity. Direct simulations at high Reynolds number would be performed, and in these case other numerical methods would be more suitable than direct simulations, as large-eddy-simulations or Reynolds stress model.

Bibliography

Bredberg, J.: 2001, On two-equations eddy-viscosity models, *Technical Report 01/8*, Chalmers Univerisy of Technology, Goteborg, Sweden.

Cherukat, P., Na, Y. and Hanratty, T. J.: 1998, Direct numerical simulation of a fully developed turbulent flow over a wavy wall, **11**, 109–134.

Choi, H. S. and Suzuki, K.: 2005, Large eddy simulation of turbulent flow and heat transfer in a channel with one wavy wall, *Int. J. Heat Fluid Flow* **26**, 681–694.

Dellil, A. Z., Azzi, A. and Jubran, B. A.: 2004, Turbulent flow and convective heat transfer in a wavy wall channel, *Heat and Mass Transfer* **40**, 793–799.

Gibson, M. M. and Dafa'Alla, A. A.: 1995, Two-equation model for turbulent wall flow, *AIAA J.* **33**, 1514–1518.

Gresho, P. M.: 1990, On the theory of semi-implicit projection methods for viscous incompressible flow and its implementation via a finite element method that also introduces a nearly consistent mass matrix. Part 1: theory, *Int. J. Numerical Methods in Fluids* **11**, 587–620.

Hudson, J. D.: 1993, *The effect of a wavy boundary on turbulent flow*, PhD thesis, University of Illinois.

Hudson, J. D., Dykhno, L. and Hanratty, T. J.: 1996, Turbulence production in flow over a wavy wall, **20**, 257.

Kader, B. A. and Yaglom, A. M.: 1972, Heat and mass transfer laws for fully turbulent wall flows, *ijhmt* **15**, 2329–2351.

Kawamura, H., Abe, H. and Matsuo, Y.: 2004, Surface heat-flux fluctuation in a turbulent channel flow up to $\mathrm{Re}_\tau = 1020$ with $\mathrm{Pr} = 0.025$ and 0.71, *Int. J. Heat Fluid Flow* **25**, 404–419.

Kawamura, H., Ohsaka, K., Abe, H. and Yamamoto, K.: 1998, Dns of turbulent heat transfer in channel flow with low to medium-high prandtl number fluid, *Int. J. Heat Fluid Flow* **19**, 482–491.

Kays, W. M.: 1994, Turbulent prandtl number - where are we?, *ASME Journal of Heat Transfer* **116**, 284–295.

Kozuka, M., Seki, Y. and Kawamura, H.: 2009, Dns of turbulent heat transfer in a channel flow with a high spatial resolution, *Int. J. Heat Fluid Flow* **30**, 514–524.

Kuhn, S., Wagner, C. and von Rohr, P. R.: 2008, The influence of wavy walls on the transport of a passive scalar in turbulent flows., **9**(10), 1–17.

Maaß, C. and Schumann, U.: 1996, Direct numerical simulation of separated turbulent flow over a wavy boundary, *in* E. H. Hirschel (ed.), *Flow simulation*

with high-performance computers, Vieweg, DLR, Institut fur Physik der Atmosphare D-82230 Oberpfanffenhofen, Germany.

Menter, F. R.: 1993, Zonal two equation k-ω turbulence models for aerodynamic flows, *AIAA Paper 93-2906* .

Moser, R., Kim, J. and Mansour, N.: 1999, Direct numerical simulation of turbulent channel flow up to $\mathrm{Re}_\tau = 590$, *Phys. Fluids* **11**(4), 943–945.

Na, Y., Papavassiliou, D. and Hanratty, T.: 1999, Use of direct numerical simulation to study the effect of prandtl number on temperature fields, *Int. J. Heat Fluid Flow* **20**, 187–195.

Patankar, S., Liu, C. and Sparrow, E.: 1977, Fully developed flow and heat transfer in ducts having streamwise-periodic variations of cross-sectional area, *ASME Journal of Heat Transfer* **99**, 180–186.

Patel, V., Cohn, J. and Yoon, J.: 1991, Turbulent flow in a channel with a wavy wall, *Journal of Fluids Engineeering* **113**, 579–586.

Pope, S.: 2000, *Turbulent flows*, Cambridge University Press, New York.

Rossi, R.: 2010, A numerical study of algebraic flux models for heat and mass traansport simulation in complex flows, *Int. J. Heat Mass Transfer* **53**, 4511–4524.

Stalio, E.: 2002/2003, *Direct numerical simulation of heat transfer enhancing surfaces*, PhD thesis, Università degli studi di Bologna.

Suga, K.: 2004, Improvement of a second moment closure for turbulent obstacle flow and heat transfer, *Int. J. Heat Fluid Flow* **25**, 776–784.

Wang, C., Jang, Y. and Leschziner, M. A.: 2004, Modelling two- and three-dimensional separation from curved surfaces with anisotropy resolving turbulence closures, *Int. J. Heat Fluid Flow* **25**, 499–512.

Younis, B., Weigand, B. and Spring, S.: 2007, An explicit algebraic model for turbulent heat transfer in wall-bounded flow with streamline curvature, *J. Heat Transfer* **129**, 425–433.

Zilker, D. and Hanratty, T.: 1979, Influence of the amplitude of a solid wavy wall on a turbulent flow. part 2. separated flows, *J. Fluid Mech.* **90**, 257–271.